Earth-Science Reviews 244 (2023) 104514

Contents lists available at ScienceDirect

Earth-Science Reviews

journal homepage: www.elsevier.com/locate/earscirev

Cycling and behavior of ^{230}Th in the Arctic Ocean: Insights from sedimentary archives

Tengfei Song [a,*], Claude Hillaire-Marcel [a], Yanguang Liu [b,c], Bassam Ghaleb [a], Anne de Vernal [a]

[a] Geotop, Université du Québec à Montréal, C.P. 8888, Montréal, QC H3C 3P8, Canada
[b] Key Laboratory of Marine Geology and Metallogeny, First Institute of Oceanography, Ministry of Natural Resources, Qingdao 266061, China
[c] Laboratory for Marine Geology, Pilot National Laboratory for Marine Science and Technology, Qingdao 266061, China

ARTICLE INFO

Keywords:
Thorium-230
Arctic Ocean
Chronostratigraphy
Paleoclimatology
Paleoceanography
Late Quaternary

ABSTRACT

Some studies have used excesses of ^{230}Th ($^{230}Th_{xs}$) in marine cores from low sedimentation rate sites for the setting of a late Pleistocene stratigraphy, but the temporal and spatial variability of $^{230}Th_{xs}$ fluxes in the Arctic Ocean remains poorly understood. In this paper, we review all available ^{230}Th data from the Arctic Ocean to document the regional $^{230}Th_{xs}$ behavior within the geological time frame of the latest glacial/interglacial cycles. We evaluate the potential roles of bathymetry, sedimentological regimes, and geochemical properties of the sediment in relation to $^{230}Th_{xs}$ fluxes. The $^{230}Th_{xs}$ inventories in the sediment accumulated since the Last Glacial Maximum suggest that $^{230}Th_{xs}$ fluxes are linked to the sea-ice regime, brine production rate and sinking, organic carbon fluxes, ice-rafting pathways, seawater exchange between the Arctic, Atlantic, and Pacific oceans, nepheloid transportation, and possibly other unidentified factors. During “warm” intervals, the development of “ice factories” over shelves and enhanced detrital and organic matter fluxes related to high sea levels and high summer insolation conditions constitute major parameters governing $^{230}Th_{xs}$-records. During glacials, under a perennial ice cover or ice shelf, $^{230}Th_{xs}$ was partly exported through Fram Strait into the Nordic Seas, and possibly partly built up in the water column, depending on the ventilation rate of the deep-water masses. At the sea floor over slopes and ridges, the winnowing of fine fractions and brines-related compounds by deep currents leads to post-sedimentary redistributions of $^{230}Th_{xs}$. These features do not invalidate chronostratigraphic inferences made using $^{230}Th_{xs}$-records in sediments but shed light on their use and limitations. Sedimentary profiles of $^{230}Th_{xs}$ allow the identification of interglacial-interstadial and glacial stages in low sedimentation rate settings. This remains valid for sediments encompassing from recent to Marine Isotope Stage 11 (MIS 11), with some reservations depending on the sedimentary characteristics of the site considered. The $^{230}Th_{xs}$ records have been initially proposed for the setting of an “extinction age” assigned to the final decay of the excess within the one-sigma uncertainty of its estimate. We show here that this extinction ages may vary between ~200 to ~420 kyr, mostly depending on the site-specific relationship between ^{230}Th deposition and sedimentary regime, and on any potential post-depositional effects, which may include redox-driven U mobility and $^{230}Th_{xs}$ losses linked to fine sediment fractions winnowing.

1. Introduction

Thorium-230 (^{230}Th) produced by dissolved and radioactive uranium (U) in the water column and accumulated into the sediment as an excess ($^{230}Th_{xs}$) over its fraction carried by detrital minerals, has often been used for normalizing sedimentary fluxes in the global oceans on the basis of a constant ^{230}Th flux model (cf. Francois et al., 2004; Costa et al., 2020). Nonetheless, this constant model is incompatible in the Arctic Ocean mainly because i) ^{230}Th scavenging in the Arctic Ocean is highly constrained by the sea ice cover, especially during glacials (e.g., Ku and Broecker, 1965; Huh et al., 1997; Strobl, 1998; Not and Hillaire-Marcel, 2010; Gusev et al., 2013; Hillaire-Marcel et al., 2017; Geibert et al., 2021; Xu et al., 2021; Purcell et al., 2022); ii) boundary scavenging of ^{230}Th may occur in the context of the wide Arctic continental shelf areas (e.g., Edmonds et al., 2004; Valk et al., 2020); iii) potential ^{230}Th export toward the Nordic Seas through Fram Strait (e.g., Moran et al., 2005; Hoffmann et al., 2013; Luo and Lippold, 2015; Hillaire-Marcel et al., 2017; Kipp et al., 2021).

* Corresponding author.
E-mail address: song.tengfei@outlook.com (T. Song).

https://doi.org/10.1016/j.earscirev.2023.104514
Received 17 January 2023; Received in revised form 16 May 2023; Accepted 19 July 2023
Available online 23 July 2023

In parallel, some investigations addressed the potential use of $^{230}Th_{xs}$ in sedimentary records for the setting of a chronostratigraphy spanning the late Quaternary, starting with the pioneering work of Ku and Broecker (1965). Peaking values of $^{230}Th_{xs}$ in cored sequences were accordingly assigned to interglacial or interstadial intervals (e.g., Strobl, 1998; Not and Hillaire-Marcel, 2010; Gusev et al., 2013; Hillaire-Marcel et al., 2017; Purcell et al., 2022). In this respect, a striking feature of the $^{230}Th_{xs}$ distribution in sedimentary sequences is the widely observed "subsurface" $^{230}Th_{xs}$ peak (Huh et al., 1997), which was tentatively assigned to the last deglaciation by Hoffmann and McManus (2007), based on ^{14}C-derived chronologies (Darby et al., 1997; Poore et al., 1999a, 1999b). This peaking "subsurface" $^{230}Th_{xs}$-value is generally higher than that of the surface sample and was thought to be related to sediment focusing due to the rapid sea level rise at the end of the last deglaciation (Hoffmann and McManus, 2007) or some $^{230}Th_{xs}$ intensifications associated with an extremely low sedimentation rate (Geibert et al., 2022). Hoffmann and McManus (2007) concluded that $^{230}Th_{xs}$ sedimentary fluxes, as estimated from ^{14}C-based chronologies, had been in balance with the production of this isotope in the water column (henceforth the "^{230}Th-rain") since the Marine Isotope Stage 3 (MIS 3). In view of recent findings by Hillaire-Marcel et al. (2022a), which invalidates the ^{14}C-derived chronology used by Hoffmann and McManus (2007), this conclusion must now be revised. More recent studies suggest that the "subsurface" $^{230}Th_{xs}$ peak should be assigned to the early MIS 3 (Not and Hillaire-Marcel, 2010; Hillaire-Marcel et al., 2017; Purcell et al., 2022), possibly in relation to some build-up of ^{230}Th in the water column during the preceding MIS 5d–4 interval (Hillaire-Marcel et al., 2022b).

In some of these recent studies, the radioactive decay of $^{230}Th_{xs}$ to values within one sigma uncertainty of its calculation in sedimentary cores, was used for the setting of a "benchmark age" or "extinction age" (Not and Hillaire-Marcel, 2010; Hillaire-Marcel et al., 2017; Purcell et al., 2022). Purcell et al. (2022) also demonstrated that the correlation of $^{230}Th_{xs}$ peaks between marine sequences differing by as much as a factor 5 in their sediment accumulation rate, was sufficiently robust to set a $^{230}Th_{xs}$-based stratigraphy spanning the last few climatic cycles (see also Geibert et al., 2021).

This $^{230}Th_{xs}$-based chronostratigraphy disagrees with chronological schemes based on ecostratigraphic considerations (e.g., Backman et al., 2009) and the Mn-cyclostratigraphy proposed by Jakobsson et al. (2000). This issue falls beyond the scope of the present study, but has been discussed in several recent papers (e.g., Xiao et al., 2021, 2022; Hillaire-Marcel and de Vernal, 2022).

Aside from the above features of ^{230}Th-behavior in the Arctic Ocean, the mechanism related to the low to near-nil $^{230}Th_{xs}$ accumulation in layers deposited during glacial stages is so far under debate. Geibert et al. (2021) assumed that near-nil $^{230}Th_{xs}$ accumulation resulted from the absence of ^{230}Th production due to the replacement of marine water by U-poor freshwater below a thick ice shelf. This assumption was challenged as several pieces of evidence show that seawater exchange between the Arctic and the Atlantic oceans continued during glacials (Spielhagen et al., 2022) and that the production of ^{230}Th was more certainly reduced but not suspended (Hillaire-Marcel et al., 2022b). Instead, for several other authors, the very low burial rates of $^{230}Th_{xs}$ during glacial stages would result from a reduced production below thick ice shelves, thus a reduced marine water column, adding to reduced scavenging with the scarce and sporadic accumulation of coarse material during short ice streaming and iceberg-rafting events (Not and Hillaire-Marcel, 2010; Hillaire-Marcel et al., 2017, 2022b; Xu et al., 2021; Purcell et al., 2022).

The above summary of studies about $^{230}Th_{xs}$ in Arctic Ocean marine sequences illustrates that its behavior, in relation to the specific hydrography, ice conditions, and sedimentology features remains insufficiently documented. Some general features of ^{230}Th behavior in the world oceans are well established. The strongly particle-reactive ^{230}Th ensuing from the dissolved ^{234}U decay is rapidly removed from the water column by fine particles (Bacon and Anderson, 1982). In the central Arctic Ocean, where aeolian dust flux is low (cf. Stein, 2008), terrestrial and marine dissolved organic matter, as well as fine organic and inorganic particles delivered by seasonal sea ice, are major scavengers of trace metals, including ^{230}Th (e.g., Baskaran, 2005; Hillaire-Marcel et al., 2017; Charette et al., 2020; Liguori et al., 2021). At sites from the central Arctic Ocean, away from the continental margin, sedimentary fluxes linked to ice-rafting deposition (IRD) are low, the present interglacial being often represented by a few centimeters of partly sorted detrital and biogenic material (e.g., de Vernal et al., 2020). Other processes, such as lateral transportation (Chen et al., 2021), winnowing of fine particles by sinking brines (Osterkamp and Gosink, 2013) and turbidity or contour currents (cf. Mosher and Boggild, 2021), and early diagenetic ferromanganese coatings may also impact $^{230}Th_{xs}$ fluxes at the sea floor and its sedimentary fate (Hoffmann and McManus, 2007; Not and Hillaire-Marcel, 2010; Hillaire-Marcel et al., 2017). Analyses of soluble and particulate phases of ^{230}Th in the water column also indicate that other factors may interfere. They include isopycnal transportation in strongly stratified water masses (Pavia et al., 2020), ventilation rates of water masses (e.g, flux and residence time of the Atlantic Water in the Arctic Ocean; cf. Wefing et al., 2020; Richards et al., 2022), and hydrothermal plumes (e.g., Valk et al., 2018, 2020; Gdaniec et al., 2020).

Building on these earlier studies, we intend to further document the behavior of ^{230}Th in the context of the Arctic Ocean. Special attention will be paid to the distribution and inventory of $^{230}Th_{xs}$ in sedimentary sequences. Using all published $^{230}Th_{xs}$ records, we intend to demonstrate in particular that two robust benchmark ages can be retained: the inception of MIS 3 and the "extinction" age of $^{230}Th_{xs}$. At the time scale of the Last Glacial Maximum (LGM) to recent, we will examine the $^{230}Th_{xs}$ inventories vs the bathymetry, geochemistry, and other sedimentological features. We will also look deeper into ^{230}Th scavenging in the Arctic Ocean, into its linkage to fine particle and organic compound fluxes, thus its relationship with sea ice production rates and subsequent brine fluxes. At last, at the Milankovitch time scale, we will explore how sea level and solar insolation changes govern $^{230}Th_{xs}$ fluxes at the sea floor, whereas its sedimentary fate might be further modified by the deep sea and diagenetic processes.

2. Background setting

The vast and shallow continental shelves (Jakobsson et al., 2012; Fig. 1A) serve as an important source of terrestrial particles toward the deep Arctic Ocean. Under high sea levels, i.e., during interglacial and/or interstadial periods, coastal erosion, wind, wave, and tidal forces lead to the resuspension of fine particles over shelves. Part of the suspended particle matter is frozen in seasonal sea ice and redistributed along the surface circulation routes, mainly through the Transpolar Drift (TPD) toward the Fram Strait, and the Beaufort Gyre (BG) in the western Arctic Ocean (Fig. 1A). The concentration of suspended particle matter in sea ice has been measured to range from 10 to 660 $mg.L^{-1}$, depending on the location and distance from the coast (Eicken, 2004, and reference therein).

The intermediate- and deep-water currents of the Arctic Ocean depict velocities generally below 6 $cm.s^{-1}$ (Galt, 1967; Hunkins et al., 1969), but could reach up to 20 $cm.s^{-1}$ in eddies extending from 100 m to at least 712 m on the Amundsen Basin side of the Lomonosov Ridge (Woodgate et al., 2001). Turbidity currents tend to be frequent, especially during glacials, leading to the potential winnowing of fine particles (Boggild and Mosher, 2021; Mosher and Boggild, 2021). Moreover, "katabatic flows of dense cold brines" (Osterkamp and Gosink, 2013) and high salinity water flow over ridges between the Amerasian basin and the Eurasian basin (cf. Jones et al., 1995), may also contribute to the winnowing of fine particles.

As a result, large amounts of small-size particles (<51 μm; up to 60 $\mu g.L^{-1}$; Xiang and Lam, 2020) and of particulate organic carbon (POC;

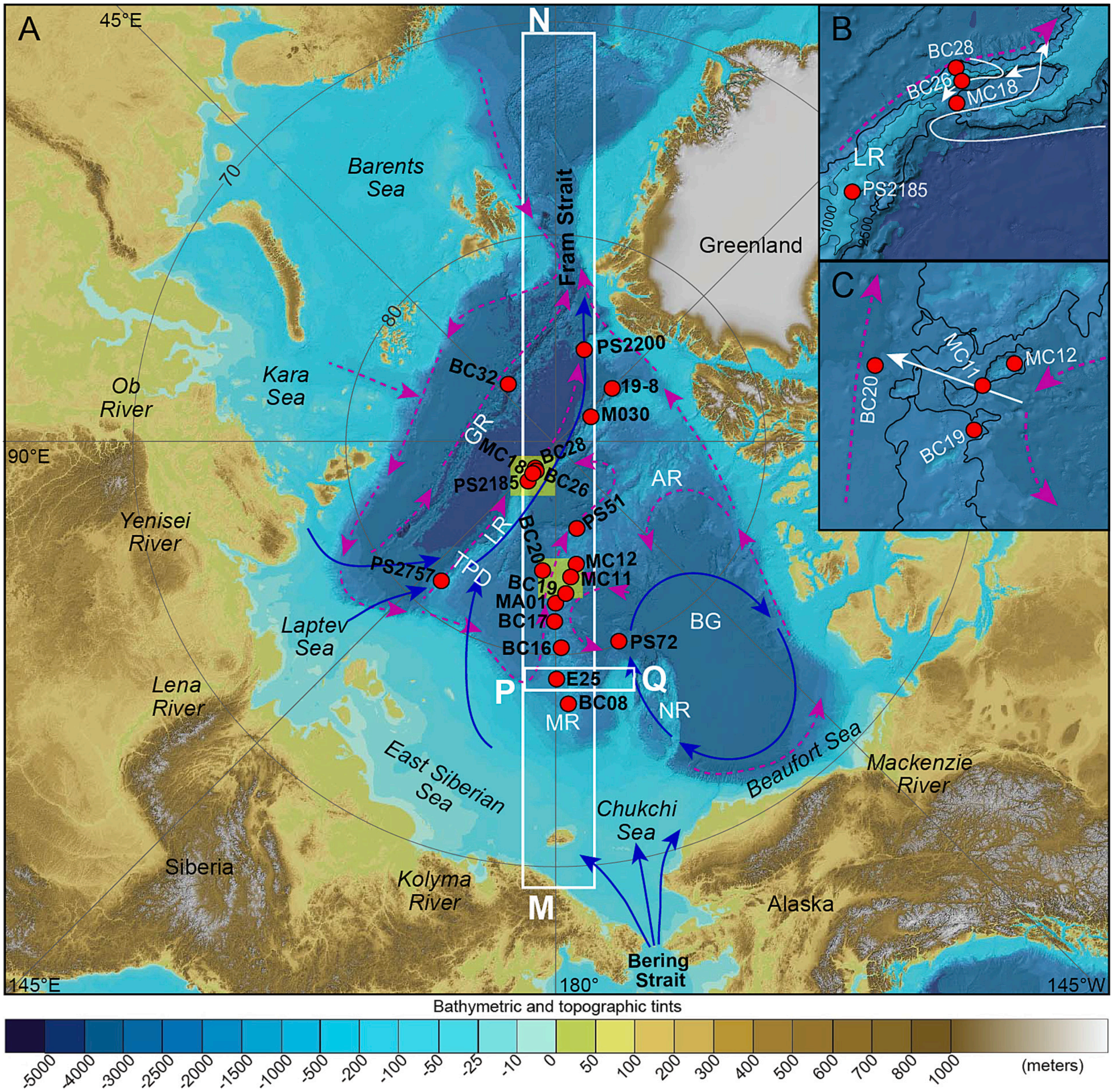

Fig. 1. A) Bathymetric map of the Arctic Ocean and major circulation features. Red dots: location of all cited cores (from Somayajulu et al., 1989; Huh et al., 1997; Strobl, 1998; Hoffmann and McManus, 2007; Not and Hillaire-Marcel, 2010, 2012; Hoffmann et al., 2013; Hillaire-Marcel et al., 2017; Geibert et al., 2021; Xu et al., 2021; Purcell et al., 2022; Song et al., 2022a); blue arrows: major surface circulation pathways; purple dashed arrows: intermediate and deep currents pathways (Rudels, 2011; Mosher and Boggild, 2021); AR: Alpha Ridge; BG: Beaufort Gyre; GR: Gakkel Ridge; LR: Lomonosov Ridge; MR: Mendeleev Ridge; NR: Northwind Ridge; TPD: Transpolar Drift. B) Closer view of sites from the Lomonosov Ridge, central Arctic Ocean, with intermediate currents paths (white arrows) based on Björk et al. (2007, 2010). C) Closer view of sites from northern Mendeleev Ridge, with the Canadian Basin Deep Water path in white arrows (Rudels et al., 2012). M-N: section along 180°E; P-Q: cross-section over core Arc7-E25 (hereafter named E25). The names of the cited cores are abbreviated in the map. The full names are provided in the main text. (For interpretation of the references to colour in this figure legend, the reader is referred to the web version of this article.)

up to 4 μmol.L^{-1}), are laterally transported and redistributed basin-wide through sea ice rafting and deep currents. They are also displaced within the intermediate and benthic nepheloid layers toward deep basins (Benner et al., 2005; Vetrov and Romankevich, 2019a; Xiang and Lam, 2020; Schulz et al., 2021). The δ^{13}C-value of POC is lower than −26‰ in the central Arctic Ocean, suggesting significant terrestrial supplies from river discharge (e.g., Xiang and Lam, 2020), whereas it averages ~ −24‰ in continental margin areas likely due to high marine primary productivity favored by seasonal sea ice opening (Bröder et al., 2016; Xiang and Lam, 2020). Lobbes et al. (2000) estimated that about 10^{13} g of organic carbon (OC) was released annually into the Arctic Ocean by the 12 major Russian rivers, with the dissolved organic carbon (DOC) fraction accounting for more than 90% of the total OC. DOC concentrations are high in the surface waters of the Arctic Ocean, especially of the central Lomonosov Ridge area, with peaking values above 100 μmol.L^{-1} (Vetrov and Romankevich, 2019b). In the intermediate and deep waters, DOC content ranges from ~54 to 64 μmol.L^{-1} (Wheeler et al., 1996; Benner et al., 2005), except in the Canada Basin where mean DOC concentrations are ~20 μmol.L^{-1} (Vetrov and Romankevich, 2019b). As a whole, the terrestrial DOC contributes to ~14 to 24% of the DOC budget of the Arctic Ocean (Benner et al., 2005). With the ongoing permafrost thawing and coastal erosion, terrestrial organic matter transport to the Arctic Ocean is expected to increase significantly (Abbott et al., 2014; Haugk et al., 2022).

The Arctic Ocean water masses are strongly stratified. Its surface layer, between 0 and ~ 50 m, the Polar Mixed Layer (Aagaard et al., 1981), is characterized by a low salinity related to sea ice melt in summer and freshwater discharge. The properties of the underlying halocline layer (about 50 to 200 m) are strongly influenced by seasonal sea ice formation and the subsequent brine production and sinking. The intermediate and deep waters in the Eurasian and Amerasian basins of the Arctic originate essentially from the Atlantic Ocean. However, dense water generated by the seasonal sea ice formation and brine production could also penetrate down to 300–400 m (Ivanov and Golovin, 2007). The mixture of Atlantic Water and sinking brines leads to the formation of an isopycnal layer within the 27.9–28.08 sigma theta (σ_θ) density range at a water depth of ~300 to 1500 m (Ivanov et al., 2004; Rogge et al., 2022) and possibly as deep as ~2000 m according to numerical models (Fu, 2022).

During glacial periods, under low sea levels, continental shelves were mostly exposed and/or glaciated. The northern margins of the two major ice sheets of the Northern Hemisphere, the Eurasian Ice Sheet and Laurentide Ice Sheet, directly impacted the Arctic Ocean (Stein et al., 2017). In addition, an East Siberian Ice Shelf/Ice Sheet, located in the East Siberian-Chukchi Sea Borderland, may have been active during several late Pleistocene glaciations (e.g., Niessen et al., 2013). This ice cover has produced scouring over the seafloor at water depths of up to 1 km (e.g., Polyak et al., 2001; Jakobsson et al., 2010; Niessen et al., 2013). Recently, it was hypothesized that, below such an ice shelf, freshwater would have replaced marine water in the deep Arctic basins and the Nordic Seas, at least during MIS 4 and 6 (Geibert et al., 2021). This hypothesis has been challenged (Spielhagen et al., 2022; Hillaire-Marcel et al., 2022b). Nonetheless, during glacials, more likely during ice advance and retreat intervals, sporadic and short sedimentary pulses occurred, linked to iceberg-rafting/ice streaming (Purcell et al., 2022) or to downslope processes (Ye et al., 2020).

3. Dataset and source

This study is based on published datasets or datasets available in the PANGAEA archives. A summary of data available for each study site (sedimentology, geochemistry) is provided in the Supplementary Material tables. A few sites have been discarded from this study due to i) the loss of core top sediments, thus the lack of data over an undefined time frame (e.g., site AF-00-07 from Gusev et al., 2013), ii) too-low numbers of U-Th measurements ($n < 10$; e.g., most sites from Somayajulu et al., 1989), iii) some large gaps in sampling intervals (e.g., up to 20 cm at site T3-63-1 of Ku and Broecker, 1965). The IRD contents are based on wet sieving, whereas clay contents are from laser diffraction measurements.

The conventional calculation of $^{230}Th_{xs}$ has been summarized by Costa et al. (2020). It consists in subtracting the lithologic and authigenic ^{230}Th fractions from the total based on the assumption that steady terrestrial particle supplies through time, thus a constant $^{232}Th/^{238}U$ ratio. However, significant variations of the $^{232}Th/^{238}U$ ratio were documented in sedimentary sequences from the Arctic Ocean, thus resulting in large uncertainties in the estimated $^{230}Th_{xs}$ (Geibert et al., 2021). Here, an approach recently proposed by Purcell et al. (2022) was used to calculate the $^{230}Th_{xs}$. It is summarized as follows:

$$A^{230}Th_{xs} = A^{230}Th - AU_{mean}$$

where A = activity of the specific isotope and AU_{mean} = the mean ^{234}U activity, or if not applicable, the mean ^{238}U activity.

Because of minute uranium losses with the preferential departure of ^{234}U due to the oxidation of the sediment that increases through time (see Supplementary Material section 2), calculating $^{230}Th_{xs}$ vs the mean ^{238}U activity may provide a better estimate of the ^{230}Th excess inherited from the initial ^{230}Th-rain downcore. However, considering the negligible offset between ^{234}U and ^{238}U activities in all records compiled (= 0 ± 0.08 dpm.g^{-1}; 1σ; n = 426), using ^{238}U activity for estimating $^{230}Th_{xs}$ would not modify significantly the overall $^{230}Th_{xs}$ distribution reported here (see also Purcell et al., 2022 about this issue).

The dry bulk density (ρ_d; DBD) in core PS51/038-4, PS2185-3/6, PS2200-5, and PS2757-6/8 (hereafter named PS51, PS2185, PS2200, PS2757, respectively) has been calculated from bulk density (ρ_w) data, based on porosity as follows: ($\rho_d = (\rho_w$ - (porosity * $\rho_{seawater}$)). For core HLY0503-11MC (hereafter named MC11) and the top 25 cm of core PS87/030-1/3 (hereafter named M030), it was calculated from dry weight sediment versus initial sampling volume data. For the lower section of core M030, it was estimated from a logarithmic trendline based on the core top dataset: $\rho_d = 0.95 + 0.19 * \log(x)$; where x is the core depth in centimeters (see Hillaire-Marcel et al., 2017). This equation provides a density value at the high range of the available datasets (see Fig. A.1). The ρ_d of cores 19-8, PL94-AR-BC08–32, Arc5-MA01, HLY0503-12MC & 18MC (hereafter named 19-8, BC08–32, MA01, MC12, MC18, respectively) was then estimated using the mean DBD data of 1.09 ± 0.16 g.cm^{-3} (± 1σ; n = 2129; see Fig. A.1).

The $^{230}Th_{xs}$ inventories were calculated as follows:

$$\sum{}^{230}Th_{xs} = \sum_i \left[(\rho_d)_i{}^* \, Ai^* \, \Delta Xi\right]$$

Where $\sum^{230}Th_{xs}$ is the total $^{230}Th_{xs}$ inventory, $(\rho_d)_i = \rho_d$ of ith the depth interval; A_i = the activity of the interval; ΔX_i = the thickness of ith depth interval.

When calculated from either ^{234}U or ^{238}U, $^{230}Th_{xs}$ inventories do not differ significantly (see Fig. A.2).

The extinction depth of $^{230}Th_{xs}$ is reached when:

$$ln\left(A^{230}Th\right) - ln\left(A^{234}U\right) \le \left[(\sigma_{230})^2 + (\sigma_{234})^2\right]^{1/2}$$

i.e., when $^{230}Th_{xs}$ falls within the quadratic sum of errors for its estimate.

The extinction age of $^{230}Th_{xs}$ at one sigma uncertainty could then be estimated based on the slope of the ln(A$^{230}Th_{xs}$) line and the half-life of ^{230}Th (~75.6 kyr; Cheng et al. (2013)). Under interglacial conditions, the theoretical ^{230}Th-rain, which is its production in the water column, was estimated using the following equation after Suman and Bacon (1989): ^{230}Th-rain (dpm.cm^{-2}.kyr^{-1}):

$$\sim [0.00263^* \, (D - 200)] + (200^* \, 0.00258)$$

where D is the water depth in meters; dpm stands for disintegrations per minute.

The equation assumes a mean salinity of ~34.2 psu in the surface water layer (the upper 200 m) vs 34.9 in the deep waters of the Arctic Ocean, which is practically identical to the mean world ocean salinity (e.g., Fournier et al., 2020).

The production of ^{230}Th under full glacial conditions is based on the assumption that the Arctic Ocean was covered by an ~800 m-thick ice shelf with an ~130 m-thick freshwater layer during the peaking glacial intervals (Hillaire-Marcel et al., 2022b). Ice shelf thicknesses during distinct glacial spans were estimated proportionally to the LR04 benthic foraminifera oxygen isotope stack of Lisiecki and Raymo (2005). However, uncertainties about the relationship with global ice volume (e.g., Raymo et al., 2018) arise from the lack of any $\delta^{18}O$ stack for the Arctic Ocean. The mean glacial ^{230}Th production would then only account for approximately 60% of the interglacial production, using the international bathymetric chart of the Arctic Ocean (IBCAO; Jakobsson, 2002) corrected for sea level changes estimated from the LR04 stack (see Lisiecki and Stern, 2016).

Radiocarbon ages of large sets of foraminifer shells must be used with caution especially at sites with very low sediment accumulation rates, as documented by Hillaire-Marcel et al. (2022a). They nonetheless provide chronological boundaries within or beyond the radiocarbon time scale. All published ^{14}C ages of the study sites were recalibrated (see Table A.2) using MARINE13 (cf. Reimer et al., 2013), as MARINE20 is not recommended for polar oceans studies due to the large uncertainty of their marine radiocarbon concentration (Heaton et al., 2020). A large array of ΔR-values can be found in the literature about the Arctic Ocean. We use here the value of 440 ± 138, from MARINE13. It is compatible with estimates from Hanslik et al. (2010) for the Holocene and from Pearce et al. (2017) for the Chukchi Sea (~300 yr and 477 ± 60 yr, respectively). We did not use the larger value of 1000 yr proposed by Hanslik et al. (2010) for pre-Holocene samples as they could be biased by the benthic mixing of foraminifer shells between the MIS 3 and Holocene layers (Hillaire-Marcel et al., 2022a).

4. Results and discussion

4.1. $^{230}Th_{xs}$ inventories

Under steady-state conditions, with constant ^{230}Th fluxes to the sea floor and constant sediment accumulation rates, $^{230}Th_{xs}$ inventories should follow a logarithmic curve driven by the radioactive decay of the isotope. Significant departures from this theoretical pattern indicate that steady-state conditions are not fulfilled (Fig. 2). Most sites show an increase in their $^{230}Th_{xs}$-inventory from the core top, with a slope well above that of a logarithmic function. This "acceleration" may be linked to a sedimentary hiatus during MIS 2 and underlying peaking $^{230}Th_{xs}$ values during MIS 3 (Fig. 2; e.g., Not and Hillaire-Marcel, 2010; Hillaire-Marcel et al., 2017).

On a longer time scale, most curves show a stepwise increase with plateaus likely corresponding to stadial and/or glacial stages (MIS 5d–4, MIS 6, and MIS 8 when recorded), and increases to interstadial/interglacial intervals (MIS 1, 3, 5e, and 7; Fig. 2C, D). An asymptotic trend is finally depicted at sites where the $^{230}Th_{xs}$ "extinction depth" has been reached.

A closer look at sites along the TPD and BG tracks, where $^{230}Th_{xs}$-inventories have almost reached an asymptotic value (Fig. 2C, D), i.e., when $^{230}Th_{xs}$ values fall within error bars of their estimate, shows inventories inversely proportional to the distance from the Russian shelves (Fig. 3; see also Purcell et al., 2022). Site BC26 depicts a unique feature that will be discussed later in Chapter 4.5.

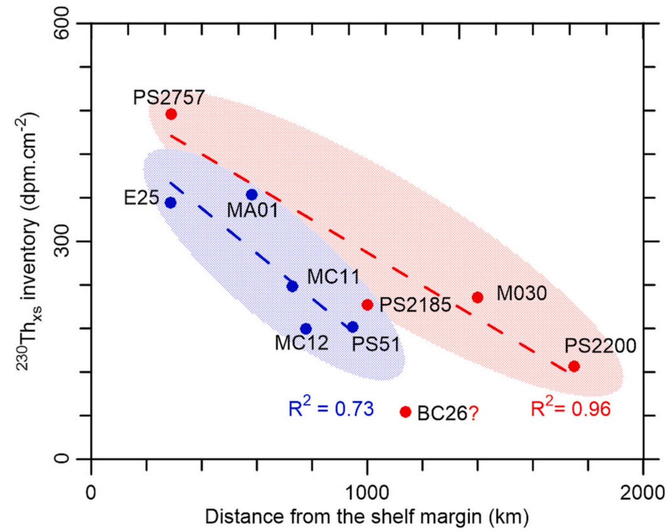

Fig. 3. $^{230}Th_{xs}$ inventories at sites where an asymptotic value has been approximately reached vs the distance from the Russian margin. Two clusters can be identified along the surface circulation patterns: BG-cluster (in blue) and TPD-cluster (in red). (For interpretation of the references to colour in this figure legend, the reader is referred to the web version of this article.)

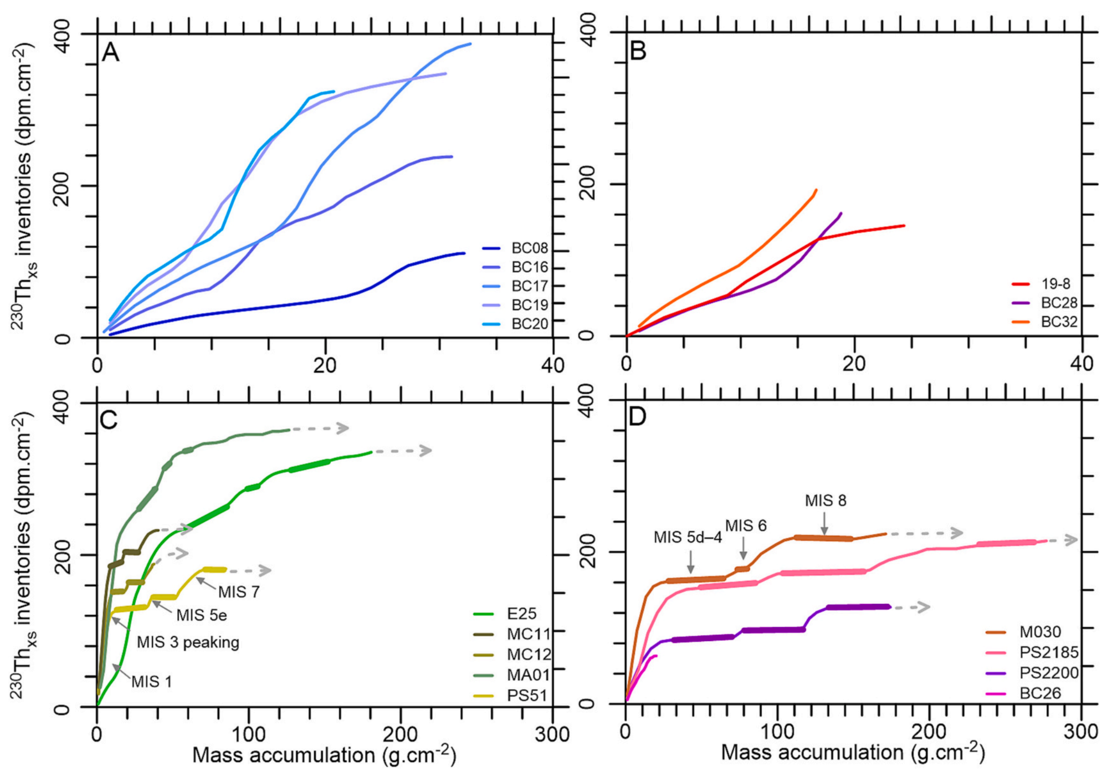

Fig. 2. $^{230}Th_{xs}$ inventories vs sediment mass accumulation at low sedimentation rate sites (<2 cm.kyr^{-1}). Here, sediment mass accumulation is used as the x-axis to avoid $^{230}Th_{xs}$ inventory biases related to the variability of sediment density downcore. Upper graphs A and B: sequences spanning MIS 3–1; lower graphs C and D: low accumulation rate sites with sequences spanning several climatic cycles; left graphs A and C: sites from the western Arctic Ocean mainly influenced by the BG; right graphs B and D: sites from the eastern Arctic Ocean influenced by the TPD. Line thickenings illustrate gaps or reduced $^{230}Th_{xs}$ burial rates during glacial intervals. Sites PS2757 and MC18 are not illustrated here as they depict significantly higher accumulation rates (>2.5 cm.kyr^{-1}) and $^{230}Th_{xs}$ inventories (>500 dpm.cm^{-2}) (see Figs. A.3 and A.4).

4.2. $^{230}Th_{xs}$ extinction depth and age

Estimates of $^{230}Th_{xs}$ extinction depths and ages in the Arctic Ocean are mentioned in very few studies (Not and Hillaire-Marcel, 2010; Hillaire-Marcel et al., 2017; Purcell et al., 2022), as they can only be calculated at sites where the $^{230}Th_{xs}$ inventory curve has reached its asymptotic value, thus, after three intervals with abrupt increases (see Fig. 2C, D). So far, among the available $^{230}Th_{xs}$ records, only seven fulfill this condition. Their $^{230}Th_{xs}$ extinction ages vary from ~200 kyr to 420 kyr, depending on the uncertainties estimated from the deviation standard (one sigma) of the slope of the ln(A^{230}Th) line and mean ^{234}U activity (Fig. 4). Within glacial layers, due to the low $^{230}Th_{xs}$ values, often within the error bar of their calculation, the estimated ages depict large uncertainties, especially those based on low analytical precision (alpha counting) and with low sampling depth resolution (Fig. 4; Table A.1).

4.3. $^{230}Th_{xs}$ distribution as a chronostratigraphic tool

Following the approach of Not and Hillaire-Marcel (2010), Hillaire-Marcel et al. (2017), and Purcell et al. (2022), we tentatively assigned peaking $^{230}Th_{xs}$-values of all cores from the central Arctic Ocean low sedimentation sites (lower panel in Fig. 5) to MIS 1, 3, 5e, 7, and also to MIS 9 and 11, where $^{230}Th_{xs}$ of these intervals are still measurable. The core top $^{230}Th_{xs}$ peak assigned to MIS 1 is difficult to distinguish from that of MIS 3 at several sites from the central Arctic Ocean due to the sedimentary hiatuse during MIS 2, and because it might be reduced or missing when the sediment surface has not been perfectly recovered. The MIS 3 interval depicts the maximum $^{230}Th_{xs}$ value at all sites (cf. the "subsurface maximum peak" of Huh et al., 1997). Deeper downcore, the MIS 5e $^{230}Th_{xs}$ values, when corrected for radioactive decay (i.e., multiplied by ~3), do not differ significantly from those of MIS 1 when it is distinguished from the MIS 3 peak, but seem lower than that of MIS 7 after correction for radioactive decay.

Using a ^{14}C-based age model, Hoffmann and McManus (2007) proposed that the subsurface $^{230}Th_{xs}$ maximum observed throughout all cores from the Arctic Ocean (Fig. 5) was due to some sediment focusing during the rapid sea level rise of the last deglaciation. However, they also considered that their age model is questionable due to benthic

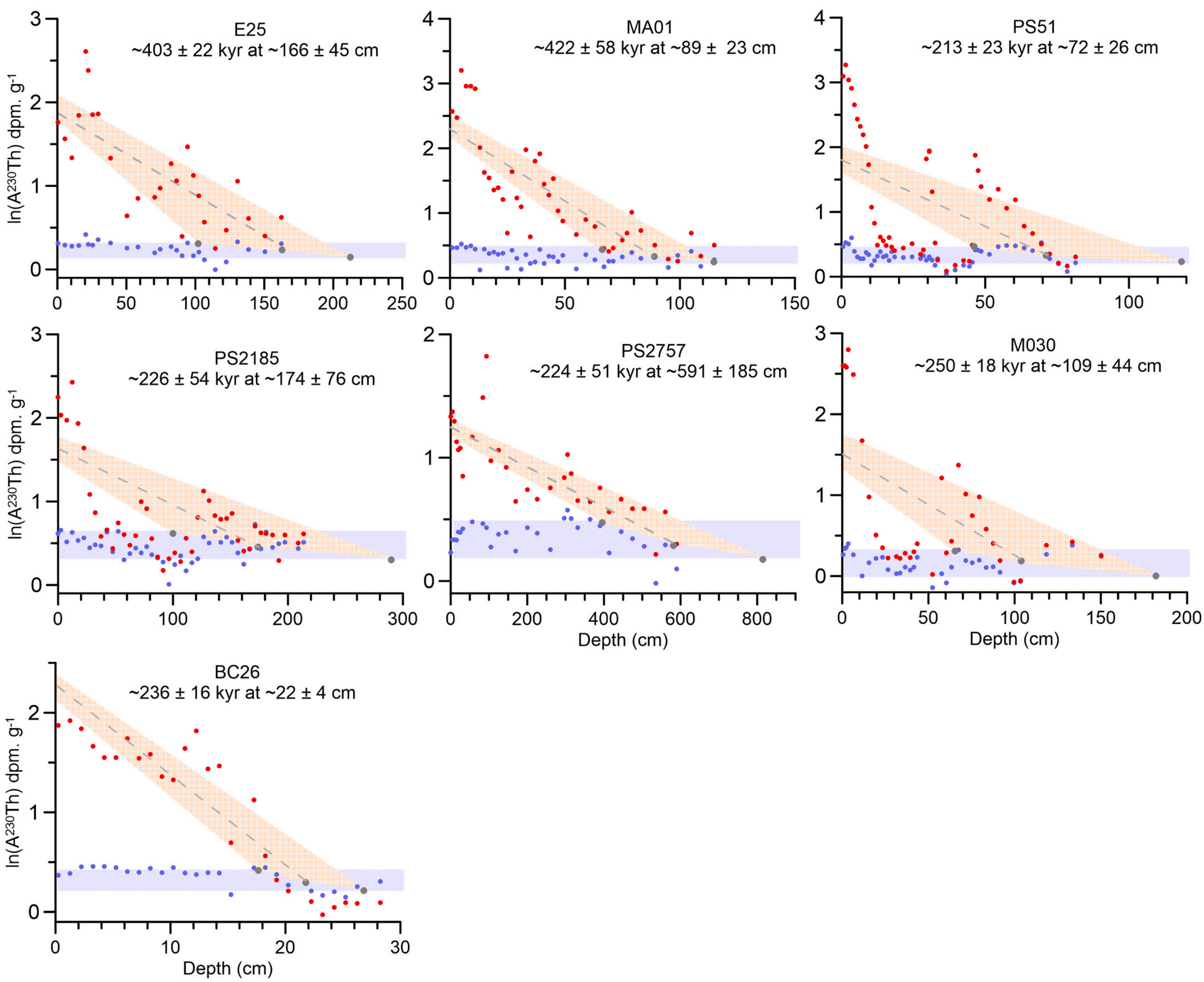

Fig. 4. ^{230}Th extinction age and depth estimates using a constant decay model for the seven sequences with suitable resolution and time span (data from Strobl, 1998; Not and Hillaire-Marcel, 2010; Hoffmann et al., 2013; Hillaire-Marcel et al., 2017; Geibert et al., 2021; Xu et al., 2021; Purcell et al., 2022; Song et al., 2022a). Blue dot: ln(A^{234}U); blue shadow area: supported ln(A^{230}Th) estimated based on the standard deviation of ln(A^{234}U); red dot: ln(A^{230}Th); grey dashed line: linear regression of ln(A^{230}Th); orange shadow area: standard deviation of the linear regression line. ^{230}Th extinction ages and their depths uncertainties are indicated below core numbers. (For interpretation of the references to colour in this figure legend, the reader is referred to the web version of this article.)

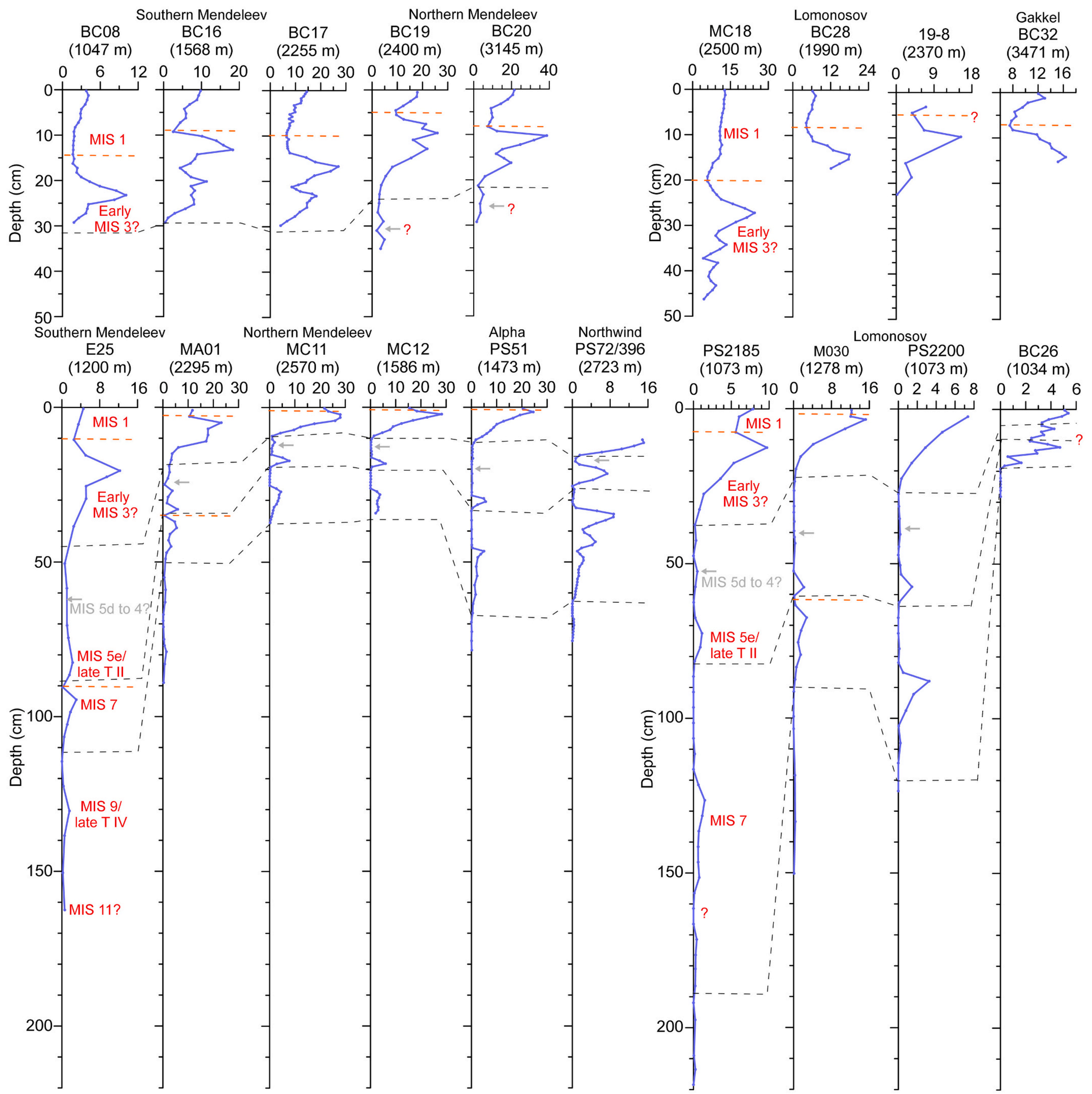

Fig. 5. $^{230}Th_{xs}$ (in dpm.g^{-1}) distribution in sedimentary sequences of the Arctic Ocean. Below core names, the water depths of the coring sites are indicated. The records in the upper part of the figure encompass MIS 3 to 1. The records in the lower part of the figure span a longer time interval. The orange dashed lines point to the MIS 2 hiatus and locally recorded MIS 6 hiatus; the black dashed lines correspond to tentative depth estimates of the MIS 4/3 transition, MIS 5e/late Termination II, and MIS 7/late termination III.

mixing. Indeed, recent ^{14}C-measurements in fish otoliths from the Lomonosov Ridge demonstrate that ^{14}C-based chronostratigraphies can be biased by the mixing of MIS 3 or older fossil specimens with Holocene specimens at sites of low sedimentation rates (Hillaire-Marcel et al., 2022a). In addition to potential biological mixing, the winnowing of fine particles by contour and overflow density currents may have contributed to the merging of MIS 3 remains at the surface (Hillaire-Marcel et al., 2022a). Regardless of this feature, radiocarbon data below the impacted surface layer support the assignment of the sub-surface $^{230}Th_{xs}$ peak to MIS 3 (Hillaire-Marcel et al., 2017, 2022a).

Intervals with $^{230}Th_{xs}$ minimums are assigned to glacial/stadial stages. MIS 2 is characterized at many sites by a sedimentary hiatus, as does MIS 6 at some sites, notably along the Mendeleev and Lomonosov ridges (e.g., Not and Hillaire-Marcel, 2010; Hillaire-Marcel et al., 2017; Geibert et al., 2021, Fig. 5). As documented in Hillaire-Marcel et al. (2022a) from the ^{14}C measurements in fish otoliths, such sites may also depict the mixing of Holocene and MIS 3 fossil remains. As substages 5a and 5c do not show significant $^{230}Th_{xs}$ peaking value in all sequences analyzed so far, we assigned the low $^{230}Th_{xs}$ layer between MIS 3 and MIS 5e to a “glacial” MIS 5d–4 interval.

Purcell et al. (2022) recently documented potential late diagenetic effects leading to a redistribution of U-isotopes (^{238}U, ^{234}U), thus impacting $^{230}Th_{xs}$ values, right below the extinction age of the initial $^{230}Th_{xs}$ at site PS2757 from the southeast Lomonosov Ridge. This fractionated U mobility seems governed by redox gradients between an organic carbon-rich layer and the over-underlying oxidized layers. Thus, much care must be taken to decipher ^{230}Th excesses linked to the initial ^{230}Th "rain" from the water column vs ^{230}Th excesses due to the diagenetic relocation of its parent isotopes before the setting of any $^{230}Th_{xs}$-based stratigraphy. Here, as illustrated in Fig. 5, a $^{230}Th_{xs}$ stratigraphy could be set with some confidence for most low sedimentation rate sites, and with some ambiguity in the case of core BC26 collected close to the North Pole.

4.4. The ^{230}Th production rate in the Arctic Ocean: glacials vs interglacials/interstadials

Since the work of Huh et al. (1997), low $^{230}Th_{xs}$ burial rates in the Arctic have been associated with the presence of a thick ice cover in the Arctic Ocean. However, the processes linking ice cover and $^{230}Th_{xs}$-fluxes at the sea floor remain unclear. Linkages with IRD during ice-sheet advances and retreats were proposed (e.g., Hillaire-Marcel et al., 2017, 2022b; Xu et al., 2021; Purcell et al., 2022). Extremely low $^{230}Th_{xs}$ during MIS 4 and 6 relate to the replacement of marine water by U-depleted freshwater, leading to negligible ^{230}Th production in the water column and $^{230}Th_{xs}$-fluxes at the sea floor, as hypothesized by Geibert et al. (2021), but challenged by Spielhagen et al. (2022) and Hillaire-Marcel et al. (2022b). Given the uncertainties about the processes involved, a reassessment of the ^{230}Th production, scavenging, and burial under distinct climate conditions seems thus needed.

Due to the relatively conservative behavior of the U/salinity ratio in oxygenated ocean water (3.22 ± 0.18 ng.g^{-1} for a salinity of ~35 psu; Ku et al., 1977; see also Suman and Bacon, 1989; Not et al., 2012), the production rate of ^{230}Th in the water column of the Arctic Ocean should be proportional to salinity and depth. Following Suman and Bacon (1989), under the present-day mean bathymetry and salinity of the central Arctic Ocean (~2700 m; Jakobsson, 2002; ~34.9, Rudels and Carmack, 2022), the ^{230}Th-rain should average ~7.2 dpm.cm^{-2}.kyr^{-1} (Fig. 6). Based on $^{231}Pa/^{230}Th$ ratios in surface sediments of the modern Arctic Ocean, Moran et al. (2005) estimated that about 10% of this ^{230}Th production is exported through Fram Strait, suggesting $^{230}Th_{xs}$ fluxes at the sea floor of about 6.5 dpm.cm^{-2}.kyr^{-1} (see also Kipp et al., 2021).

During glacials, with the development of ice shelves and under low sea levels, the ^{230}Th production in the glaciated Arctic Ocean was significantly changed. Under full glacial conditions, the global sea level was ~120 m below the modern one, and an ~800 m-thick ice overlying an ~130 m freshwater layer (Hillaire-Marcel et al., 2022b) could have characterized most of the Arctic Ocean. As documented by Spielhagen et al. (2022), there were exchanges between the deep Arctic Ocean and the Atlantic Ocean through Fram Strait, thus allowing for ^{230}Th export from the Arctic Ocean. Hence, the ^{230}Th-rain in the central Arctic Ocean would have averaged ~4.5 dpm.cm^{-2}.kyr^{-1} under a saline water layer of about 1700 m thick (Fig. 6). This would represent ~40% reduction of the ^{230}Th-rain during glacials compared to interglacials. As coarse IRD is not an efficient scavenger of ^{230}Th, a significant part of the $^{230}Th_{xs}$ could have been exported through Fram Strait or partly build up in the water column, depending upon ventilation rates and seawater exchanges between the Arctic and Atlantic oceans (Fig. 6; Hoffmann et al., 2013; Luo and Lippold, 2015; Kipp et al., 2021; Hillaire-Marcel et al., 2022b). This assumption, however, does not contradict the hypothesis of Geibert et al. (2021) as most studied sites are from relatively shallow ridges, close or within reach of the ice shelf and/or its accompanying freshwater lower boundary ridges. Hence, ^{230}Th flux at the sea floor may have been reduced at shallow sites such as that of core E25 (Fig. 6).

4.5. Factors governing ^{230}Th fluxes from the water column and their sedimentary fate

The factors controlling $^{230}Th_{xs}$ scavenging rates and fluxes at the sea floor were examined based on studies of the water column (e.g., Bacon et al., 1989; Scholten et al., 1995; Edmonds et al., 1998) and sediments (e.g., Moran et al., 2005; Hoffmann and McManus, 2007; Hoffmann et al., 2013; Luo and Lippold, 2015; Hillaire-Marcel et al., 2017; Geibert et al., 2021). Water column investigations provide a snapshot of a modern-like situation, while sediment studies often used radiocarbon chronologies for flux calculation (e.g., Hoffmann and McManus, 2007; Hoffmann et al., 2013; Luo and Lippold, 2015; Hillaire-Marcel et al., 2017), which may present intrinsic biases as documented by Hillaire-Marcel et al. (2022a). Other studies refer to surface sediments without any clear information about their temporal context (e.g., Moran et al., 2005). Further examination of factors controlling $^{230}Th_{xs}$ burial rates on well-constrained time frames and at large scale thus seems relevant.

4.5.1. ^{230}Th flux at the sea floor and its burial

Aside from a consensus about maximum $^{230}Th_{xs}$ values linked to MIS 3 and recent interglacial intervals, when Arctic shelves were submerged and the summer season insolation was peaking, not much is known about the variability of $^{230}Th_{xs}$ fluxes and burial rates during the late Quaternary and at the scale of the whole Arctic Ocean. Most studies published so far were based on a limited number of sedimentary sequences, thus yielding a partial view of the issue (e.g., Huh et al., 1997; Strobl, 1998; Not and Hillaire-Marcel, 2010; Gusev et al., 2013; Hillaire-Marcel et al., 2017; Purcell et al., 2022). Here, we try to confront all published inventories of $^{230}Th_{xs}$ in post-LGM sediments with a few physical and chemical parameters, including water depth, sedimentation rate, clay and IRD fluxes, mean grain size (Φ-value), and OC flux.

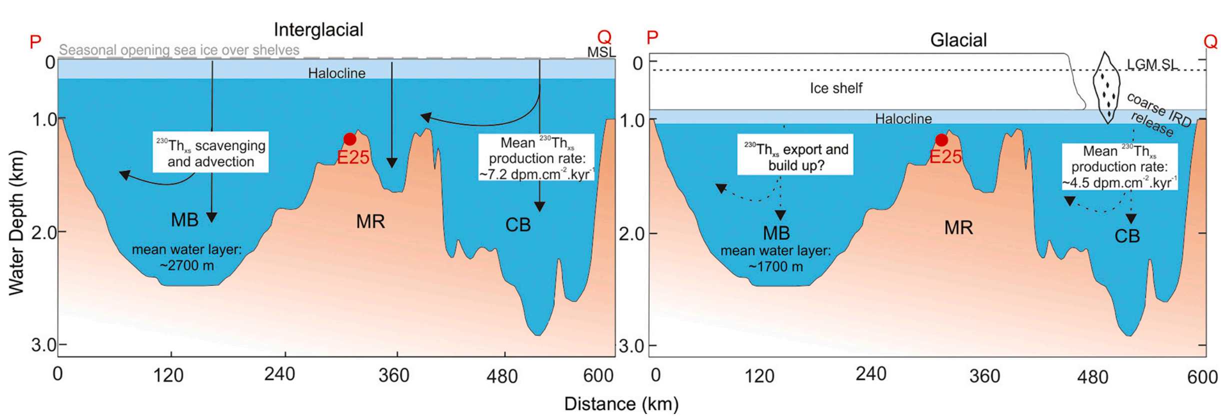

Fig. 6. Sketch of the $^{230}Th_{xs}$ production in the Arctic Ocean during interglacial and glacial intervals. The location of section P-Q could be seen in Fig. 1A. Red dot: location of core E25. CB: Canadian Basin; MB: Makarov Basin; MR: Mendeleev Ridge; MSL: Modern Sea Level; SL: sea level. (For interpretation of the references to colour in this figure legend, the reader is referred to the web version of this article.)

Due to the difficulty of setting time boundaries in sedimentary records for time intervals older than MIS 3, we looked specifically at the post-LGM sedimentary layer, with the LGM set at the depth of the minimum $^{230}Th_{xs}$ value above the MIS 3 peak (Figs. 2, 5). This post-LGM layer mostly records Holocene sedimentation, at least over ridges where it barely exceeds 1 or 2 cm (e.g., Not and Hillaire-Marcel, 2010; de Vernal et al., 2020), with maximum calibrated ^{14}C ages of 9 kyr and maximum sedimentary fluxes during the early to middle Holocene (Hillaire-Marcel et al., 2022a). In sequences recovered from box and multi-cores, this Holocene layer is generally well recovered (e.g., Poore et al., 1999a, 1999b; Table A.2), but its recovery is far from ascertained in gravity or piston cores where surface sediments may have been lost (e.g., Gusev et al., 2013). Thus, the total number of sites used for this part of the study was reduced to 17 or less, in cases when a physical or chemical parameter was missing (Fig. 7). All cores illustrated in Fig. 7 are from low sedimentation rate sites (<2 cm.kyr^{-1}). We will look at the two high sedimentation rate sites (PS2757; MC18) independently, later on. As most of the post-LGM sediment accumulation occurred during the last 9 kyr (Not and Hillaire-Marcel, 2010; Hillaire-Marcel et al., 2022a), fluxes reported in Fig. 7 have been estimated as representing 9 kyr interval, and not the last 21 kyr elapsed since the LGM.

Some features emerge from Fig. 7. The post-LGM $^{230}Th_{xs}$ inventory correlates with the bathymetry of the coring site and the OC flux, whereas it anti-correlates with the coarse fraction content (Φ-value). In comparison with the ^{230}Th-rain, the $^{230}Th_{xs}$ burial rate is mostly in deficit, consistent with earlier assumptions about ^{230}Th export since the LGM (e.g., Moran et al., 2005; Hoffmann et al., 2013; Luo and Lippold, 2015). However, as documented in Hillaire-Marcel et al. (2022a), evidence of sediment winnowing over ridges by "katabatic flows of dense cold brines" (Osterkamp and Gosink, 2013), and/or turbidity, density-driven contour currents (cf. Jones et al., 1995; Björk et al., 2007, 2010; Boggild and Mosher, 2021; Mosher and Boggild, 2021), could also account for some $^{230}Th_{xs}$-loss over these ridge sites. As discussed below, some deep intra-basin sites record relatively very high $^{230}Th_{xs}$ inventories likely due to re-sedimentation of winnowed sediments from ridges.

The weak correlation between $^{230}Th_{xs}$ and clay fluxes is based on a low number of observations and does not permit discarding the role of clay in scavenging. However, it seems reasonable to assume that in the "sediment-starved" Arctic Ocean, thorium scavenging is primarily controlled by organic compounds in part adsorbed onto fine particle surfaces (Baskaran et al., 2003; Zhang et al., 2021). For example, at a site such as that of core M030, the mean sedimentation rate is less than ~4 mm.kyr^{-1} (Hillaire-Marcel et al., 2017). Clays represent ~24% of the sediment (Table A.4). The accumulation rate of fine scavenging mineral particles is low on a thousand-year time scale, which is significantly longer than the 20 to 40 yrs residence time of ^{230}Th in the Arctic Ocean as estimated by Scholten et al. (1995) and Trimble et al. (2004). The activity of $^{230}Th_{xs}$ value at the top of core M030 is ~12 dpm.g^{-1}. The ^{230}Th scavenger would be the DOC, in particular, specific fractions of colloids (Baskaran et al., 2003), which also play a substantial role in coagulating and transporting trace metals (e.g., Fe, Mn, Co, Ni; Guo et al., 2000; Pokrovsky et al., 2014; Krickov et al., 2019).

Beyond ^{230}Th production in the water column, the major parameter governing $^{230}Th_{xs}$ fluxes at the floor of the deep Arctic Ocean and its burial rates seems related to organic matter. Marine DOC is the major scavenger of trace metals in the western Arctic Ocean, whereas both marine and terrestrial DOC are effective carriers in the Eurasian basin (Williford et al., 2022). Under the influences of several physical and biological processes (e.g., coagulation, mixing, gravitational settling, ecosystem structure and food-web interactions; Roca Martí, 2017), $^{230}Th_{xs}$-enriched organic matter aggregations would sink to the seafloor. The positive relationship between $^{230}Th_{xs}$ inventory and sedimentation rate, and OC flux in the TPD cluster relates to the riverine discharge and seasonal sea ice production on the Siberian continental shelf (Suman and Bacon, 1989; Wheeler et al., 1996; Benner et al., 2005; de Vernal et al., 2020; Fadeev et al., 2021; Rogge et al., 2022; Williford et al., 2022). On a long geological time scale, it could thus be related to high summer season insolation and high sea level conditions (Hillaire-Marcel et al., 2021).

In the BG cluster of the western Arctic Ocean (Fig. 7), DOC concentrations are lower than those of the TPD area due to weak terrestrial

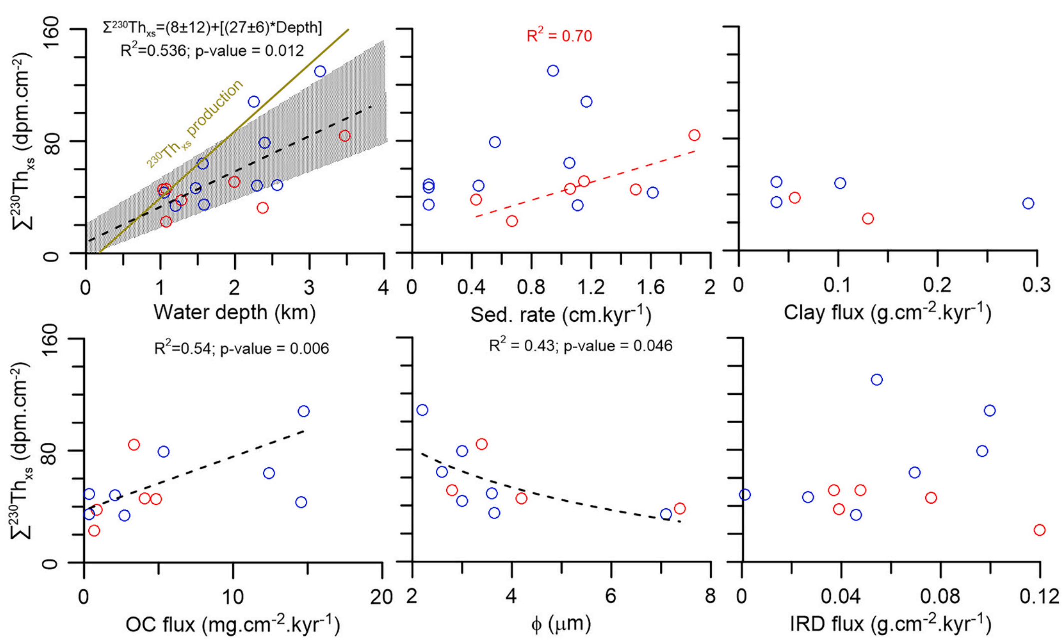

Fig. 7. The post-LGM $^{230}Th_{xs}$ inventories vs physical and chemical parameters in low sediment accumulation rate sites. Correlation coefficients and *p*-values are reported when significant. Blue circles: datasets from the BG cluster; red circles: datasets from the TPD cluster; black line: regression trend based on both datasets; olive line: estimated ^{230}Th production over the past 21 kyr; red dashed line: linear regression based on the TPD dataset; Φ: mean grain size; IRD: larger than 63 µm fractions. The sedimentation rate and all fluxes have been set assuming that the post-LGM layer mostly includes sediments deposited since 9 cal. kyr BP (see text in subchapter 4.5.1). (For interpretation of the references to colour in this figure legend, the reader is referred to the web version of this article.)

discharge from the Mackenzie River compared to Russian rivers (Stein, 2008; Vetrov and Romankevich, 2019b). However, primary productivity over the Chukchi Sea shelf is important and constitutes the major contributor to the DOC budget of the western Arctic Ocean (Williford et al., 2022). The decreasing $^{230}Th_{xs}$ inventories from the continental margin to the central western Arctic Ocean (Fig. 3) would thus be linked to the lateral transportation and progressive removal/decay of the DOC along the intermediate and benthic nepheloid layers (e.g., Xiang and Lam, 2020; Chen et al., 2021; Schulz et al., 2021).

Brines play a complementary role as they carry most of the DOC produced by sea ice algae and microfauna. The organic contents of the brine promote organic ligand complexation (Becquevort et al., 2009; Ardiningsih et al., 2021). Brine could extract and release 60 to 70% of the labile trace metals (e.g., Fe, Mn, Cd) from the dirty sea ice (Grotti et al., 2005; Evans and Nishioka, 2018, 2019). Therefore, brines could re-distribute the soluble and leachate phases $^{230}Th_{xs}$ along their advection and sinking into the central Arctic Ocean.

A few coring sites deserve specific attention. The cores MC18 and BC26 were raised ~24 nautical miles apart on the Lomonosov Ridge but at different water depths. Core BC26 is from ~1034 m on the ridge crest, and core MC18 is from ~2500 m in an intra-basin of the ridge (Fig. 1B). The post-LGM-inventories of $^{230}Th_{xs}$ in core MC18 is ~237 dpm.cm^{-2}, more than twice the ^{230}Th-rain. In opposition, the post-LGM peak is not distinguishable from that of MIS 3 in core BC26. Core BC26 depicts a highly compacted $^{230}Th_{xs}$ profile with an MIS 7 inception assigned at ~20 cm, which corresponds to the depth of the MIS 3 peak in the deeper MC18 site. We see here evidence for proximal redeposition of fine sediments and their $^{230}Th_{xs}$ and will discuss it in subchapter 4.5.2.

Another site with particular features is that of core PS2757, which is characterized by relatively high sedimentation rates (~2.6 cm.kyr^{-1}; Fig. A.4). Purcell et al. (2022) have well-documented the behavior of $^{230}Th_{xs}$ in this core. They highlighted the facts that sites with sedimentation rates exceeding a few cm.kyr^{-1} are characterized by dilution of the ^{230}Th from the water column by detrital ^{230}Th supplies and that the possible diagenetic U mobility would make the $^{230}Th_{xs}$ approach unsuitable for estimating extinction ages, as well as for the setting a $^{230}Th_{xs}$-based stratigraphy.

4.5.2. *Post-depositional process impacting $^{230}Th_{xs}$ records*

Aside from radioactive decay and vertical ^{230}Th rain, the post-depositional processes that could alter $^{230}Th_{xs}$ records include: i) late diagenetic processes along major redox boundaries linked to high organic carbon content layers, as documented from core PS2757 by Purcell et al. (2022); ii) supplies from glacial erosion by thick ice shelves (e.g., Jakobsson et al., 2016); iii) sediment winnowing by deep currents and redeposition (Björk et al., 2007; Not and Hillaire-Marcel, 2010).

In the Lomonosov Ridge area, the post-LGM $^{230}Th_{xs}$-inventories at sites BC26 and BC28 located on the crest of the ridge are close to equilibrium or in deficit with the corresponding ^{230}Th-rain values (Fig. 8; Table A.3). Comparatively, core MC18 raised from the Intra Basin of the ridge, and core PS2185 collected away from the deep-water exchange channel (Fig. 1B) depict strong excesses in ^{230}Th-inventories. This feature may be associated with winnowing and redeposition processes driven by the active deep-water exchange between the Makarov and Amundsen basins (Björk et al., 2007, 2010), especially at site BC26 that is influenced by the Canadian Basin Deep Water (Björk et al., 2010). The $^{230}Th_{xs}$-enriched fine components of sites BC26 and BC28 would have been laterally transported toward deeper sites, such as MC18. Similar features are observed in the western Arctic Ocean. Sites MC11 and MC12 are located at the northern tip of Mendeleev Ridge, in the pathway of the Canadian Basin Deep Water (Fig. 1C; Rudels et al., 2012). They depict deficits in their post-LGM $^{230}Th_{xs}$ inventories vs the corresponding ^{230}Th-rain values (Fig. 8; Table A.3). In opposition, site BC20, lying deeper in the Makarov Basin, and the sheltered site BC19 show ^{230}Th-inventories in balance with the ^{230}Th-rain (Figs. 1C, 8; Table A.3). Unfortuanately, a quantitative assessment of the $^{230}Th_{xs}$ removal and redeposition relating to deep water exchanges is still out of reach due to the rare datasets available, especially from the deep Arctic Basins.

4.6. *Paleoclimatic and paleoceanographic implications from $^{230}Th_{xs}$ records*

In contrast to the sediment-focusing model which has been used to interpret the subsurface $^{230}Th_{xs}$ peak (Hoffmann and McManus, 2007), Geibert et al. (2022) suggested that the subsurface $^{230}Th_{xs}$ peak might be linked to extremely low sedimentation rate considering that "*Even fine particle fluxes generating sedimentation rates < 1 mm/1000 years lead to >*

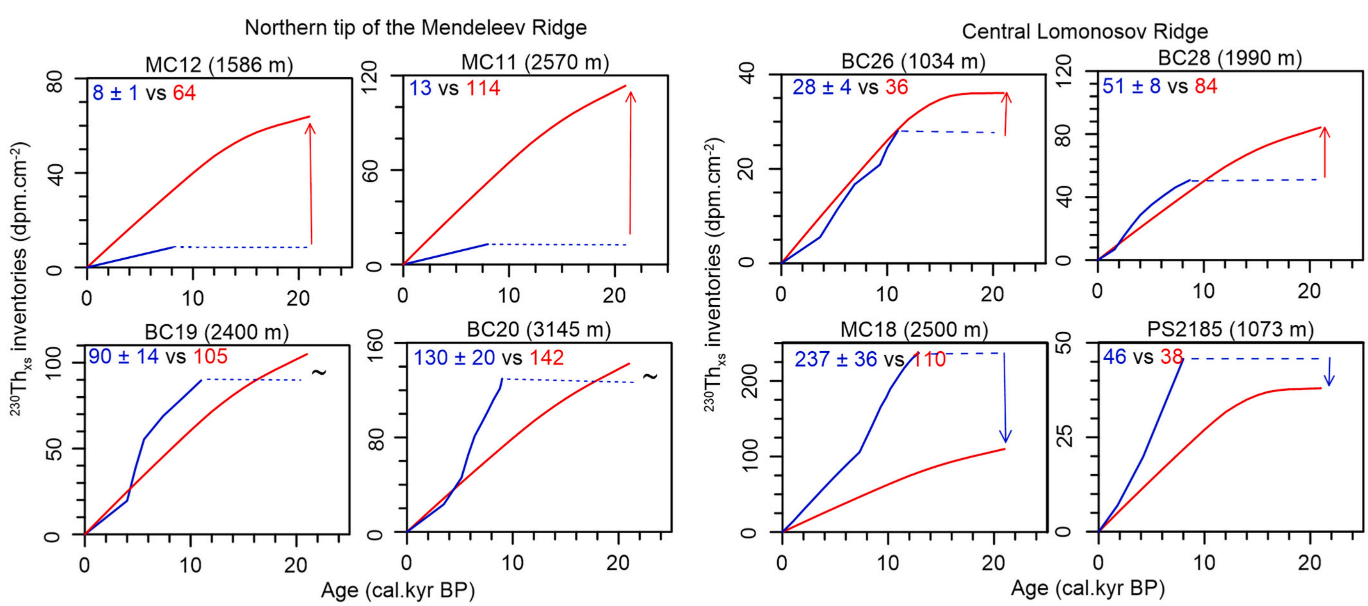

Fig. 8. Post-LGM $^{230}Th_{xs}$ inventories vs ^{230}Th production in the overlying water column (^{230}Th-rain) in cores from Lomonosov and Mendeleev ridge areas. Inventories are estimated to mostly represent sediment and $^{230}Th_{xs}$ accumulation during the last ~9 ka; the ^{230}Th-rain is calculated since the end of the LGM (~18 ka). Blue lines and numbers: $^{230}Th_{xs}$ inventory in cores; red lines and numbers: ^{230}Th-rain; blue arrows: $^{230}Th_{xs}$ inventory above the ^{230}Th-rain; red arrows: $^{230}Th_{xs}$ inventory below the ^{230}Th-rain. (For interpretation of the references to colour in this figure legend, the reader is referred to the web version of this article.)

100-fold ^{230}Th concentrations elsewhere (Yang et al., 1986)". However, this assumption is in contradiction with the thick sediment layer deposited during MIS 3 (> 10 cm; Fig. 5). In our view, the sub-surface $^{230}Th_{xs}$ peak indicates enhanced sea ice rafting deposition, thus seasonally open sea ice over largely submerged shelves (Xiao et al., 2015). Such conditions were met under i) the relatively high sea level (~ −40 m to −50 m) that was reached during MIS 3 (Pico et al., 2020; Dalton et al., 2022), ii) the high summer insolation of the ~54 to 49 kyr interval (Hillaire-Marcel et al., 2021), and iii) the shrub tundra vegetation between 54 and 51 kyr that was reconstructed at the proximity of the Lena River delta by Zimmermann et al. (2017). However, all factors accounting for the maximum $^{230}Th_{xs}$ of this early MIS 3 interval still remain not fully elucidated. Hillaire-Marcel et al. (2022b) proposed that some build-up of ^{230}Th in the water column of the Arctic Ocean, under a resilient ice shelf spanning the MIS 5d–4 interval, may have contributed to the enhanced scavenging rates of $^{230}Th_{xs}$ during the early MIS 3. Enhanced DOC fluxes during this interval might have also played a role as DOC is an efficient scavenger of trace metals (e.g., Williford et al., 2022). Interestingly, the DOC contents in ice wedges from the Lena Delta by Wetterich et al. (2020) suggest that DOC concentrations in the MIS 3 layer (~367 mg.L^{-1}) were about one-order magnitude higher than those of the Holocene layer (~34 mg.L^{-1}), which is compatible with organic inputs from terrestrial vegetation (Zimmermann et al., 2017) through the Lena River that presently contributes ~50% of the DOC supplied by Russian rivers (Lobbes et al., 2000). Hence, a high terrestrial DOC flux toward the Arctic Ocean some 55–50 kyr ago might have greatly contributed to a high ^{230}Th-scavenging rate during this early MIS 3 interval.

A critical feature of all available records is the relatively low $^{230}Th_{xs}$ in sediments of the Last Interglacial (MIS 5e) compared to MIS 7. The longer duration of MIS 7 than MIS 5e, its high summer insolation, and its three high sea-level phases might explain a better recording of MIS 7 than MIS 5e in the Arctic Ocean sedimentary sequences as proposed by Hillaire-Marcel et al. (2021). Because of chronostratigraphic issues, as evoked in the introduction of the present paper, notably for the Last Interglacial (see also Kageyama et al., 2021; Hillaire-Marcel and de Vernal, 2022; West et al., 2023), there is no unequivocal information about the paleoceanography of MIS 5e for the central Arctic Ocean. Nevertheless, reliable stratigraphical schemes are available from the Nordic Seas, where all studies report a shorter, mostly cooler MIS 5e interval in comparison with the Holocene (Rasmussen et al., 2003; Oppo et al., 2006; Bauch and Erlenkeuser, 2008; Van Nieuwenhove and Bauch, 2008). On this basis, assuming a short and mostly cool Arctic Ocean during MIS 5e, a lesser $^{230}Th_{xs}$ recording of the interval is possible. According to Wetterich et al. (2016), "*…the isotopic composition (d^{18}O, dD) [and pollen content] of the Buchchagy ice-wedge [Laptev Sea cost] indicates [MIS 5] winter conditions colder than during the MIS 3 […], harsher summer conditions and rather similar vegetation as during the MIS 2 stadial.*"

It is important to highlight the fact that, by itself, the low $^{230}Th_{xs}$ characterizing the MIS 5e in the Arctic Ocean, does not necessarily indicate a shorter or cooler interval in comparison with the Holocene. As evoked above in reference to the study by Hillaire-Marcel et al. (2022a), the winnowing of fine $^{230}Th_{xs}$-barrier particles, by density-driven and contour currents, occurs over ridges. Therefore, active circulation and high rates of sea ice production and sinking brines could also result in low $^{230}Th_{xs}$ in sediments from the ridge summits. Under such a scenario, the low $^{230}Th_{xs}$ value of the interval assigned to MIS 5e could well point to warm conditions and high brine production rates during MIS 5e, in contradiction with what could be proposed solely based on some direct proportionality between ^{230}Th fluxes and climate conditions. Such a scenario involving the winnowing of fine particles by density-driven bottom currents can be supported by some arguments pointing to highly dynamic sea ice conditions during the Last Interglacial: i) the MIS 5e experienced a significantly higher sea level (up to ~9 m vs the Present; Kopp et al., 2009; Dutton et al., 2015; ii) thus, the flux of relatively "warm" and low salinity Pacific waters through Bering Strait was potentially higher by ~50% than at present (Song et al., 2022b), with impact on the freshwater budget and sea ice regime in the Arctic Ocean (Karami et al., 2021). Enhanced circulation and higher brine production rates could then account for a loss of $^{230}Th_{xs}$ and of its fine carrier particles and compounds through winnowing processes. Thus, we suggest keeping open the debate about paleoclimate conditions in the Arctic Ocean during MIS 5e until more direct evidence from proxies is available.

4.7. Overview of the glacial vs interglacial ^{230}Th cycling in the Arctic Ocean

In addition to the main parameters governing the fate of ^{230}Th production in the Arctic Ocean discussed above, a large array of other processes may also interfere with its scavenging, fluxes within the basin and at the sea floor, effective burial, and post-depositional evolution. They range from land erosion and river runoff, coastal erosion, sea ice and brine dynamics, slope processes, isopycnal transportation, reversible scavenging, deep currents, deep ocean circulation and exchanges with other oceans, hydrothermal plumes (e.g., Valk et al., 2018, 2020; Gdaniec et al., 2020; Pavia et al., 2020; Chen et al., 2021), aside from other potential factors not yet documented. An overview of major processes so far identified, which may have variable impacts in time and space, is provided in Table 1 and illustrated in Fig. 9.

4.7.1. The submerged continental margin during interglacials/interstadials

Aside from the direct linkages between ^{230}Th production and shelf water salinity, primary productivity, river runoff, terrestrial DOC, and fine particle fluxes, shallow currents control the dispersal of fine particles and colloids, thus ^{230}Th-boundary scavenging processes (e.g., Nozaki et al., 1981; Roy-Barman, 2009; Kuzyk et al., 2013). Coastal and shelf processes also include permafrost thawing, groundwater discharge, coastal erosion, and sediment resuspension induced by tidal, wave, and wind forces (Holmes et al., 2002; Abbott et al., 2014; Wegner et al., 2015; Haugk et al., 2022). In fine, ^{230}Th-scavenging particles and compounds are dispersed toward the central Arctic Ocean through sea ice-rafting, eddies, and currents (Fig. 9; Roy-Barman, 2009; Kipp et al., 2018; Xiang and Lam, 2020; Rogge et al., 2022). Due to the large shelf area of the Arctic Ocean, boundary scavenging is a critical parameter, especially under high sea levels, when shelves are submerged (cf. Edmonds et al., 2004; Moran et al., 2005; Gdaniec et al., 2020). Seasonal sea ice production also interferes as fragile sea ice dwelling from the sea surface down to 25 m, could capture suspended particles (Ito et al., 2019, 2021; Drits et al., 2021). At last, brines related to sea ice formation sink on the shelf floor (down to ~300–400 m in the Laptev shelf; e.g., Ivanov and Golovin, 2007), leading to the mixing of trace metals over the shelf and their redistribution downslope (Evans and Nishioka, 2018, 2019).

4.7.2. The exposed continental margin during glacials/stadials

Under the low sea levels of glacial/stadial intervals, continental shelves were mostly exposed (Jakobsson et al., 2010, 2012), and the Bering Strait was closed (Jakobsson et al., 2017). Thus, several parameters mentioned above, such as shallow shelf currents related to the Pacific and Atlantic waters inflows, sediment resuspension, boundary scavenging, and seasonal sea ice-related processes, including primary productivity, were either strongly reduced or nil (Fig. 9; Table 1). Besides, river and continental DOC discharges were impeded by the existence of ice sheets/shelves surrounding the Arctic (Polyak et al., 2001; Jakobsson et al., 2010; Stein et al., 2017), whereas large lakes developed southward over northern Siberia (Krinner et al., 2004). Glacial advance over shelves would then carry unsorted, relatively coarse particles toward the deep basins (Purcell et al., 2022). Combining all these features, ^{230}Th scavenging on the continental shelves was practically stopped, with quasi-nil transportation of ^{230}Th-bearing particles and compounds

Table 1
Overview of factors influencing ^{230}Th cycling in the Arctic Ocean.

Parameter	Effective role	Status		Reference
		Glacial	Interglacial	
River discharge	Fine particle and DOC supplies		√	Holmes et al., 2002
Coastal erosion	Particulate supply		√	Wegner et al., 2015
Boundary scavenging	^{230}Th burial & resuspension over continental shelves	on slopes?	√	Edmonds et al., 2004; Moran et al., 2005; Kuzyk et al., 2013
Sediment resuspension over shelves	Entrainment into fragile sea ice and lateral transportation		√	Baskaran, 2005; Charette et al., 2020; Drits et al., 2021
Brines	Coagulation of organic matter with ^{230}Th adsorption		√	Evans and Nishioka, 2018, 2019; Ito et al., 2019, 2021
Seasonal sea-ice melting	Fine particle release and phytoplankton blooms		√	Kipp et al., 2018; Fadeev et al., 2021;
Ice streaming	Glacial erosion and unsorted detrital supplies	√		Polyak et al., 2001; Jakobsson et al., 2010, 2016; Purcell et al., 2022
Isopycnal transportation	Brines mixing with Atlantic Water		√	Pavia et al., 2020; Rogge et al., 2022
Hydrothermal fluid	Sporadic scavenging	√	√	Valk et al., 2018; Gdaniec et al., 2020
Pacific Water inflow	Chukchi Sea role		√	Kuzyk et al., 2013
Atlantic water inflow and deep water export	Export of ^{230}Th	√	reduced	Moran et al., 2005; Hoffmann et al., 2013; Gdaniec et al., 2020; Valk et al., 2020
Deep overflowing currents	Fine particle and compound winnowing on ridge crests		√	Björk et al., 2007, 2010; Hillaire-Marcel et al., 2022a
Reversible scavenging	Desorption at the water-sediment interface	√	√	Trimble et al., 2004; Gdaniec et al., 2020; Valk et al., 2020
Intermediate and bottom currents	Re-suspension of scavenged particles and compounds	reduced	√	Xiang and Lam, 2020; Schulz et al., 2021; Gardner et al., 2022;
Turbidity and contour currents	Winnowing of fine particles and compounds	Enhanced?	√	Mosher and Boggild, 2021

toward the central Arctic Ocean (Fig. 9).

4.7.3. The cycling of ^{230}Th in the deep Arctic Ocean during interglacials/interstadials

^{230}Th distribution in the Arctic Ocean is influenced by the sea ice-generated brines, as it does around Antarctica (Grotti et al., 2005; Becquevort et al., 2009; Ardiningsih et al., 2021). With a penetration depth of ~300–400 m, brines depict high concentrations of soluble and adsorbed phases of ^{230}Th as discussed above. They are partly mixed with the intruding Atlantic Water, forming an isopycnal layer ~300–1000 m deep (Ivanov et al., 2004). The intrusion of Atlantic Water was observed to be stronger over the past ten years, leading to the deepening of the isopycnal layer to ~1500 m, occasionally down to 2000 m (Fig. 9; Gdaniec et al., 2020; Valk et al., 2020; Fu, 2022; Rogge et al., 2022). Thus, isopycnal transportation must be considered as an important player in the redistribution of ^{230}Th in the high-latitude ocean (Pavia et al., 2020). The Arctic deep water also depicts a high soluble ^{230}Th concentration as a result of the reversible scavenging (Gdaniec et al., 2020). Hence, ^{230}Th speciation and concentration are heterogeneous within the different water layers of the Arctic Ocean.

Another important process that influences the ^{230}Th distribution in the deep Arctic Ocean is the lateral transportation within the intermediate and bottom nepheloid layers (Fig. 9; e.g., Chen et al., 2021; Schulz et al., 2021; Gardner et al., 2022; Williford et al., 2022). Following the fine particle concentration gradients from the continental slope to the central Arctic Ocean (Xiang and Lam, 2020; Williford et al., 2022), decreasing trace metal concentrations (e.g., Fe, Co, Nd) in the water column are observed (Charette et al., 2020; Liguori et al., 2021).

It has been reported that hydrothermal plumes from the Gakkel Ridge could contribute to ^{230}Th scavenging in the deep Nansen Basin (Valk et al., 2018). However, the relatively slow spreading rate and low overall hydrothermal activity (Jean-Baptiste and Fourré, 2004) lead to inferring low influence on ^{230}Th cycling at the scale of the whole Arctic Ocean.

4.7.4. $^{230}Th_{xs}$ burial in the deep Arctic Ocean during glacials

During glacial periods, turbulent mixing was mostly paused below the severe ice cover, resulting in reduced lateral transportation (Rippeth and Fine, 2022). The deep circulation might have been similarly reduced (e.g., Hillaire-Marcel et al., 2022b). Whereas, due to their low velocity (2 to 6 cm.s^{-1}; Galt, 1967; Hunkins et al., 1969), bottom currents should generally be of minor impact on the ^{230}Th$_{xs}$-rain dispersal. However, they cannot be overlooked where boundary currents are active (Woodgate et al., 2001). Such turbidity and contour currents were apparently active during glacials in the Lomonosov Ridge and Canadian Basin (Weigelt et al., 2020; Boggild and Mosher, 2021), especially under low sea levels (Mosher and Boggild, 2021). This might have led to the resuspension and removal of fine particles deposited during earlier interglacial/interstadial intervals.

5. Conclusion

One major conclusion that may be drawn from this synthesis work is that there is no simple proportionality between time and sediment or ^{230}Th$_{xs}$ deposition in the deep Arctic Ocean. No realistic time interpolation or time estimate can be made aside from the stratigraphic assignment of peaking ^{230}Th$_{xs}$-values to specific "warm" intervals and the calculation of ^{230}Th$_{xs}$ extinction age.

Without more information on ^{230}Th$_{xs}$ in deep depocenter, ^{230}Th-budgets are difficult to set, especially for glacial intervals. Overall, one may infer reduced ^{230}Th deposition during such episodes, in particular at shallow sites within reach of ice shelves or of their underlying freshwater layer (Hillaire-Marcel et al., 2022b). This would be partly compatible with the hypothesis of a "freshwater-filled" Arctic Ocean by Geibert et al. (2021). The strongest evidence for some ^{230}Th-export, at least during MIS 2, may be derived from ^{231}Pa/^{230}Th activity ratios as documented by Moran et al. (2005) or Hillaire-Marcel et al. (2017). This would imply a possibly reduced, but still active deep water circulation and exchanges with the Nordic Seas and Atlantic Ocean (cf. Spielhagen et al., 2022).

The compilation of ^{230}Th$_{xs}$ distributions and inventories in cored sequences published so far allows us to reassess the usefulness of ^{230}Th$_{xs}$ as a stratigraphic tool as proposed in earlier papers (e.g., Strobl, 1998; Not and Hillaire-Marcel, 2010; Hillaire-Marcel et al., 2017; Geibert et al., 2021; Purcell et al., 2022). Two benchmark ages could be reasonably set: i) that of the subsurface ^{230}Th$_{xs}$ peak (~53 kyr), and ii) the ^{230}Th$_{xs}$ extinction age downcore (~220 to 420 kyr). They lead to paleoceanographic inferences about the Arctic Ocean quite distinct from those using biostratigraphic markers and Mn-based cyclostratigraphy (see also Hillaire-Marcel and de Vernal, 2022) and even, radiocarbon

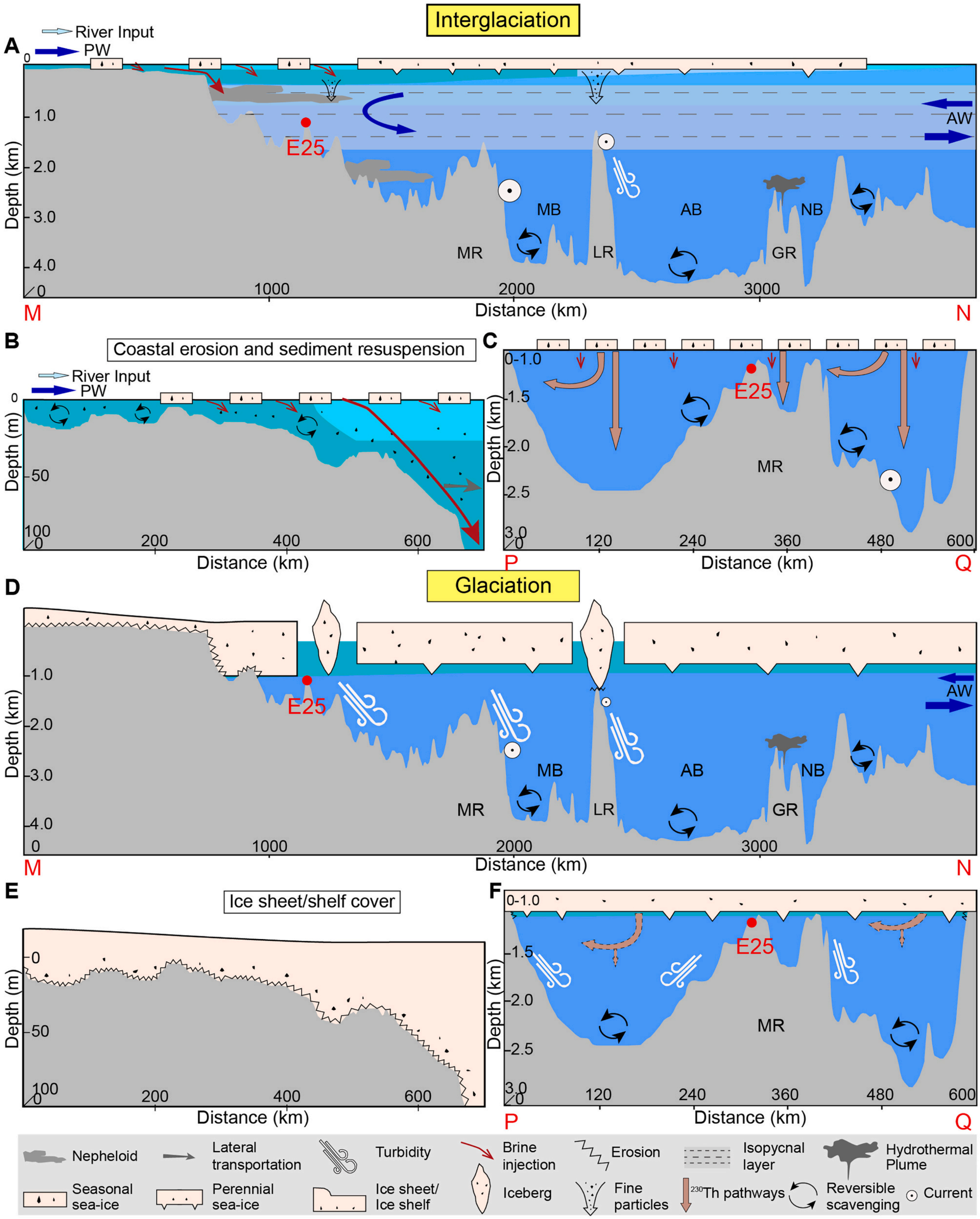

Fig. 9. Sketch of the cycling of ^{230}Th in the water column of the Arctic Ocean under different climate conditions. A, B, C): interglacial/interstadial; D, E, F) glacial/stadial; A, D): along the 180° transect of the Arctic Ocean; B, E): Siberian continental shelf; C, F): cross-section through site E25 from the southern Mendeleev Ridge. The red dot marks the location of core E25. (For interpretation of the references to colour in this figure legend, the reader is referred to the web version of this article.)

(Hillaire-Marcel et al., 2022a). However, in some cases, the $^{230}Th_{xs}$-based stratigraphy should be used with some caution, notably when the MIS 1 $^{230}Th_{xs}$ peak is not distinguishable from that of MIS 3, or when the redox-driven diagenetic processes interfere (Purcell et al., 2022).

This review highlights the importance of solar insolation and sea level in governing the cycling and sedimentation of trace metals in the Arctic Ocean, through the critical role of seasonal sea ice production and melting over submerged continental shelves (Hillaire-Marcel et al., 2021). It also documents post-depositional processes related to brine-driven deep current exchanges between the Canadian, Amundsen and Eurasian basins resulting in some $^{230}Th_{xs}$ redistribution from the ridges to the deep basins. At last, it confirms the major role of DOC, either produced by marine algae or discharged by the rivers (particularly the Lena River), in ^{230}Th-scavenging processes.

Future work could be focused on deep basins and continental margins as their inventories in ^{230}Th and ^{231}Pa could help constrain better the budgets of these isotopes during recent glacials and the MIS 3 and 5e, in particular.

CRediT authorship contribution statement

Tengfei Song: Conceptualization, Methodology, Software, Formal analysis, Writing – original draft, Writing – review & editing. **Claude Hillaire-Marcel:** Conceptualization, Methodology, Formal analysis, Supervision, Writing – review & editing, Project administration, Funding acquisition. **Yanguang Liu:** Writing – review & editing, Funding acquisition. **Bassam Ghaleb:** Methodology, Formal analysis, Writing – review & editing. **Anne de Vernal:** Writing – review & editing, Funding acquisition.

Declaration of Competing Interest

The authors declare that they have no known competing financial interests or personal relationships that could have appeared to influence the work reported in this paper.

Data availability

All the data used in this study are referenced in Table A.1 of the Supplementary Material.

Acknowledgment

This work was supported by the Natural Sciences and Engineering Research Council (NSERC) of Canada [grant number: RGPNS-2019-459035], the Regroupement Stratégique de Recherche from Fonds de Recherche du Québec Nature et Technologies (FRQNT) [grant number: 2018-RS-203300], NSERC-CREATE ArcTrain, and the National Natural Science Foundation of China [grant number: 41876070]. Thanks to Dr. Yufen Rong for her assistance with drawing the figures. The financial support from China Scholarship Council is highly appreciated by T.-F. Song. Three anonymous reviewers provided many helpful suggestions. Their input has been highly appreciated.

Appendix A. Supplementary data

Supplementary data to this article can be found online at https://doi.org/10.1016/j.earscirev.2023.104514.

References

Aagaard, K., Coachman, L.K., Carmack, E., 1981. On the halocline of the Arctic Ocean. Deep Sea Res. Part I Oceanogr. Res. Pap. 28 (6), 529–545. https://doi.org/10.1016/0198-0149(81)90115-1.

Abbott, B.W., et al., 2014. Elevated dissolved organic carbon biodegradability from thawing and collapsing permafrost. J. Geophys. Res. Biogeosci. 119 (10), 2049–2063. https://doi.org/10.1002/2014JG002678.

Ardiningsih, I., et al., 2021. Fe-binding organic ligands in coastal and frontal regions of the western Antarctic Peninsula. Biogeosciences 18 (15), 4587–4601. https://doi.org/10.5194/bg-18-4587-2021.

Backman, J., Fornaciari, E., Rio, D., 2009. Biochronology and paleoceanography of late Pleistocene and Holocene calcareous nannofossil abundances across the Arctic Basin. Mar. Micropaleontol. 72 (1–2), 86–98. https://doi.org/10.1016/j.marmicro.2009.04.001.

Bacon, M.P., Anderson, R.F., 1982. Distribution of thorium isotopes between dissolved and particulate forms in the deep sea. J. Geophys. Res. Oceans 87 (C3), 2045–2056. https://doi.org/10.1029/JC087iC03p02045.

Bacon, M.P., Huh, C., Moore, R.M., 1989. Vertical profiles of some natural radionuclides over the Alpha Ridge, Arctic Ocean. Earth Planet. Sci. Lett. 95 (1–2), 15–22. https://doi.org/10.1016/0012-821X(89)90164-7.

Baskaran, M., 2005. Interaction of sea ice sediments and surface sea water in the Arctic Ocean: evidence from excess ^{210}Pb. Geophys. Res. Lett. 32 (12), L12601. https://doi.org/10.1029/2004GL022191.

Baskaran, M., Swarzenski, P.W., Porcelli, D., 2003. Role of colloidal material in the removal of ^{234}Th in the Canada basin of the Arctic Ocean. Deep Sea Res. Part I Oceanogr. Res. Pap. 50 (10−11), 1353–1373. https://doi.org/10.1016/S0967-0637(03)00140-7.

Bauch, H.A., Erlenkeuser, H., 2008. A "critical" climatic evaluation of last interglacial (MIS 5e) records from the Norwegian Sea. Polar Res. 27 (2), 135–151. https://doi.org/10.1111/j.1751-8369.2008.00059.x.

Becquevort, S., et al., 2009. Biogeochemistry and microbial community composition in sea ice and underlying seawater off East Antarctica during early spring. Polar Biol. 32 (6), 879–895. https://doi.org/10.1007/s00300-009-0589-2.

Benner, R., Louchouarn, P., Amon, R.M.W., 2005. Terrigenous dissolved organic matter in the Arctic Ocean and its transport to surface and deep waters of the North Atlantic. Glob. Biogeochem. Cycles 19 (2), GB2025. https://doi.org/10.1029/2004GB002398.

Björk, G., et al., 2007. Bathymetry and deep-water exchange across the central Lomonosov Ridge at 88–89 N. Deep Sea Res. Part I Oceanogr. Res. Pap. 54 (8), 1197–1208. https://doi.org/10.1016/j.dsr.2007.05.010.

Björk, G., et al., 2010. Flow of Canadian basin deep water in the Western Eurasian Basin of the Arctic Ocean. Deep Sea Res. Part I Oceanogr. Res. Pap. 57 (4), 77–586. https://doi.org/10.1016/j.dsr.2010.01.006.

Boggild, K., Mosher, D.C., 2021. Turbidity currents at polar latitudes: a case study of NP-28 channel in the Amundsen Basin, Arctic Ocean. Mar. Geol. 440, 106571 https://doi.org/10.1016/j.margeo.2021.106571.

Bröder, L., et al., 2016. Fate of terrigenous organic matter across the Laptev Sea from the mouth of the Lena River to the deep sea of the Arctic interior. Biogeosciences 13 (17), 5003–5019. https://doi.org/10.5194/bg-13-5003-2016.

Charette, M. A., et al., 2020. The Transpolar Drift as a source of riverine and shelf-derived trace elements to the Central Arctic Ocean. J. Geophys. Res. Oceans 125(5), p.e2019JC015920. doi: https://doi.org/10.1029/2019JC015920.

Chen, S.Y.S., et al., 2021. On the cycling of ^{231}Pa and ^{230}Th in benthic nepheloid layers. Deep Sea Res. Part I Oceanogr. Res. Pap. 177, 103627 https://doi.org/10.1016/j.dsr.2021.103627.

Cheng, H., et al., 2013. Improvements in ^{230}Th dating, ^{230}Th and ^{234}U half-life values, and U–Th isotopic measurements by multi-collector inductively coupled plasma mass spectrometry. Earth Planet. Sci. Lett. 371, 82–91. https://doi.org/10.1016/j.epsl.2013.04.006.

Costa, K.M., et al., 2020. ^{230}Th normalization: new insights on an essential tool for quantifying sedimentary fluxes in the modern and Quaternary Ocean. Paleoceanogr. Paleoclimatol. 35 (2) https://doi.org/10.1029/2019PA003820 e2019PA003820.

Dalton, A.S., et al., 2022. The marine $\delta^{18}O$ record overestimates continental ice volume during Marine Isotope Stage 3. Glob. Planet. Chang. 212, 103814 https://doi.org/10.1016/j.gloplacha.2022.103814.

Darby, D.A., Bischof, J.F., Jones, G.A., 1997. Radiocarbon chronology of depositional regimes in the western Arctic Ocean. Deep Sea Res. Part II Top. Stud. Oceanogr. 44 (8), 1745–1757. https://doi.org/10.1016/S0967-0645(97)00039-8.

de Vernal, A., et al., 2020. Natural variability of the Arctic Ocean sea ice during the present interglacial. Proc. Natl. Acad. Sci. U. S. A. 117 (42), 26069–26075. https://doi.org/10.1073/pnas.2008996117.

Drits, A.V., et al., 2021. Influence of riverine discharge and timing of ice retreat on particle sedimentation patterns on the Laptev Sea shelf. J. Geophys. Res. Oceans 126 (10). https://doi.org/10.1029/2021JC017462 e2021JC017462.

Dutton, A., et al., 2015. Sea-level rise due to polar ice-sheet mass loss during past warm periods. Science 349 (6244), aaa4019. https://doi.org/10.1126/science.aaa4019.

Edmonds, H.N., et al., 1998. Protactinium-231 and thorium-230 abundances and high scavenging rates in the western Arctic Ocean. Science 280 (5362), 405–407. https://doi.org/10.1126/science.280.5362.405.

Edmonds, H.N., et al., 2004. ^{230}Th and ^{231}Pa in the Arctic Ocean: implications for particle fluxes and basin-scale Th/Pa fractionation. Earth Planet. Sci. Lett. 227 (1–2), 155–167. https://doi.org/10.1016/j.epsl.2004.08.008.

Eicken, H., 2004. The Role of Arctic Sea Ice in Transporting and Cycling Terrestrial Organic Matter. In: Stein, R., Macdonald, R.W. (Eds.), The Organic Carbon Cycle in the Arctic Ocean: Present and Past. Springer-Verlag, Berlin, pp. 45–53. https://doi.org/10.1007/978-3-642-18912-8_4.

Evans, L.K., Nishioka, J., 2018. Quantitative analysis of Fe, Mn and Cd from sea ice and seawater in the Chukchi Sea, Arctic Ocean. Polar Sci. 17, 50–58. https://doi.org/10.1016/j.polar.2018.07.002.

Evans, L.K., Nishioka, J., 2019. Accumulation processes of trace metals into Arctic Sea ice: distribution of Fe, Mn and Cd associated with ice structure. Mar. Chem. 209, 36–47. https://doi.org/10.1016/j.marchem.2018.11.011.

Fadeev, E., et al., 2021. Sea ice presence is linked to higher carbon export and vertical microbial connectivity in the Eurasian Arctic Ocean. Commun. Biol. 4 (1), 1–13. https://doi.org/10.1038/s42003-021-02776-w.

Fournier, S., et al., 2020. Sea surface salinity as a proxy for Arctic Ocean freshwater changes. J. Geophys. Res. Oceans 125 (7). https://doi.org/10.1029/2020JC016110 e2020JC016110.

Francois, R., et al., 2004. ^{230}Th normalization: an essential tool for interpreting sedimentary fluxes during the late Quaternary. Paleoceanography 19 (1), PA1018. https://doi.org/10.1029/2003PA000939.

Fu, C., 2022. Modelling the Atlantic Water along its Poleward Pathway into and through the Arctic Ocean. MSc Thesis. University of Alberta, Edmonton. https://doi.org/10.7939/r3-gadk-ny91.

Galt, J.A., 1967. Current measurements in the Canadian Basin of the Arctic Ocean, summer, 1965. Tech. Rep. No. 184. Dept. of Oceanography, Univ. of Washington, Seattle.

Gardner, W.D., et al., 2022. Distribution, sources, and dynamics of particulate matter along trans-arctic sections. J. Geophys. Res. Oceans 127 (6). https://doi.org/10.1029/2021JC017970 e2021JC017970.

Gdaniec, S., et al., 2020. ^{231}Pa and ^{230}Th in the Arctic Ocean: implications for boundary scavenging and ^{231}Pa/^{230}Th fractionation in the Eurasian Basin. Chem. Geol. 532, 119380 https://doi.org/10.1016/j.chemgeo.2019.119380.

Geibert, W., et al., 2021. Glacial episodes of a freshwater Arctic Ocean covered by a thick ice shelf. Nature 590 (7844), 97–102. https://doi.org/10.1038/s41586-021-03186-y.

Geibert, W., et al., 2022. Reply to 'Challenging the hypothesis of an arctic ocean lake during recent glacial episodes' by Hillaire-Marcel, et al. J. Quat. Sci. 37 (4), 568–571. https://doi.org/10.1002/jqs.3431.

Grotti, M., et al., 2005. Trace metals distributions in coastal sea ice of Terra Nova Bay, Ross Sea, Antarctica. Antarct. Sci. 17 (2), 289–300. https://doi.org/10.1017/S0954102005002695.

Guo, L., Santschi, P.H., Warnken, K.W., 2000. Trace metal composition of colloidal organic material in marine environments. Mar. Chem. 70 (4), 257–275. https://doi.org/10.1016/S0304-4203(00)00031-1.

Gusev, E.A., et al., 2013. Stratigraphy of bottom sediments in the Mendeleev Ridge area (Arctic Ocean). In: Dokl. Earth Sci. 450, 602–60.

Hanslik, D.M., et al., 2010. Quaternary Arctic Ocean sea ice variations and radiocarbon reservoir age corrections. Quat. Sci. Rev. 29 (25–26), 3430–3441. https://doi.org/10.1016/j.quascirev.2010.06.011.

Haugk, C., et al., 2022. Organic matter characteristics of a rapidly eroding permafrost cliff in NE Siberia (Lena Delta, Laptev Sea region). Biogeosciences 19 (7), 2079–2094. https://doi.org/10.5194/bg-19-2079-2022.

Heaton, T.J., et al., 2020. Marine20—the marine radiocarbon age calibration curve (0–55,000 cal BP). Radiocarbon 62 (4), 779–820. https://doi.org/10.1017/RDC.2020.68.

Hillaire-Marcel, C., de Vernal, A., 2022. A comment about" A sedimentary record from the Makarov Basin, Arctic Ocean, reveals changing middle to Late Pleistocene glaciation patterns"(Quat. Sci. Rev., 270 (2021), p. 107176) from W. Xiao, L. Polyak, R. Wang, C. Not, L. Dong, Y. Liu, T. Ma, T. Zhang. Quat. Sci. Rev. 279, 107239. https://doi.org/10.1016/j.quascirev.2021.107239.

Hillaire-Marcel, C., et al., 2017. A new chronology of late Quaternary sequences from the Central Arctic Ocean based on "extinction ages" of their excesses in ^{231}Pa and ^{230}Th. Geochem. Geophys. Geosyst. 18 (12), 4573–4585. https://doi.org/10.1002/2017GC007050.

Hillaire-Marcel, C., de Vernal, A., Crucifix, M., 2021. Sea-level and summer season orbital insolation as drivers of Arctic r-ice. arXiv preprint arXiv:2102.02067. https://doi.org/10.48550/arXiv.2102.02067.

Hillaire-Marcel, C., et al., 2022a. Challenging radiocarbon chronostratigraphies in central Arctic Ocean sediment. Geophys. Res. Lett. 49 https://doi.org/10.1029/2022GL100446 e2022GL100446.

Hillaire-Marcel, C., et al., 2022b. Challenging the hypothesis of an Arctic Ocean lake during recent glacial episodes. J. Quat. Sci. 37 (4), 559–567. https://doi.org/10.1002/jqs.3421.

Hoffmann, S., McManus, J., 2007. Is there a ^{230}Th deficit in Arctic sediments? Earth Planet. Sci. Lett. 258 (3–4), 516–527. https://doi.org/10.1016/j.epsl.2007.04.011.

Hoffmann, S., et al., 2013. Persistent export of ^{231}Pa from the deep central Arctic Ocean over the past 35,000 years. Nature 497 (7451), 603–606. https://doi.org/10.1038/nature12145.

Holmes, R.M., et al., 2002. A circumpolar perspective on fluvial sediment flux to the Arctic Ocean. Glob. Biogeochem. Cycles 16 (4). https://doi.org/10.1029/2001GB001849, 1098.

Huh, C.A., et al., 1997. Natural radionuclides and plutonium in sediments from the western Arctic Ocean: sedimentation rates and pathways of radionuclides. Deep-Sea Res. II Top. Stud. Oceanogr. 44 (8), 1725–1743. https://doi.org/10.1016/S0967-0645(97)00040-4.

Hunkins, K., Thorndike, E.M., Mathieu, G., 1969. Nepheloid layers and bottom currents in the Arctic Ocean. J. Geophys. Res. 74 (28), 6995–7008. https://doi.org/10.1029/JC074i028p06995.

Ito, M., et al., 2019. Favorable conditions for suspension freezing in an Arctic coastal polynya. J. Geophys. Res. Oceans 124 (12), 8701–8719. https://doi.org/10.1029/2019JC015536.

Ito, M., et al., 2021. Underwater frazil ice and its suspension depth detected from ADCP backscatter data around sea ice edge in the Sea of Okhotsk. Cold Reg. Sci. Technol. 192, 103382 https://doi.org/10.1016/j.coldregions.2021.103382.

Ivanov, V.V., Golovin, P.N., 2007. Observations and modeling of dense water cascading from the northwestern Laptev Sea shelf. J. Geophys. Res. Oceans 112 (C9), C09003. https://doi.org/10.1029/2006JC003882.

Ivanov, V.V., et al., 2004. Dense water cascades around the World Ocean. Prog. Oceanogr. 60, 47–98. https://doi.org/10.1016/j.pocean.2003.12.002.

Jakobsson, M., 2002. Hypsometry and volume of the Arctic Ocean and its constituent seas. Geochem. Geophys. Geosyst. 3 (5), 1–18. https://doi.org/10.1029/2001GC000302.

Jakobsson, M., et al., 2000. Manganese and color cycles in Arctic Ocean sediments constrain Pleistocene chronology. Geology 28 (1), 23–26. https://doi.org/10.1130/0091-7613(2000)28%3C23:MACCIA%3E2.0.CO;2.

Jakobsson, M., et al., 2010. An Arctic Ocean ice shelf during MIS 6 constrained by new geophysical and geological data. Quat. Sci. Rev. 29 (25–26), 3505–3517. https://doi.org/10.1016/j.quascirev.2010.03.015.

Jakobsson, M., et al., 2012. The international bathymetric chart of the Arctic Ocean (IBCAO) version 3.0. Geophys. Res. Lett. 39 (12), L12609. https://doi.org/10.1029/2012GL052219.

Jakobsson, M., et al., 2016. Evidence for an ice shelf covering the central Arctic Ocean during the penultimate glaciation. Nat. Commun. 7 (1), 10365. https://doi.org/10.1038/ncomms10365.

Jakobsson, M., et al., 2017. Post-glacial flooding of the Bering Land Bridge dated to 11 cal ka BP based on new geophysical and sediment records. Clim. Past 13 (8), 991–1005. https://doi.org/10.5194/cp-13-991-2017.

Jean-Baptiste, P., Fourré, E., 2004. Hydrothermal activity on Gakkel Ridge. Nature 428 (6978), 36. https://doi.org/10.1038/428036a.

Jones, E.P., Rudels, B., Anderson, L.G., 1995. Deep waters of the Arctic Ocean: origins and circulation. Deep Sea Res. Part I Oceanogr. Res. Pap. 42 (5), 737–760. https://doi.org/10.1016/0967-0637(95)00013-V.

Kageyama, M., et al., 2021. A multi-model CMIP6-PMIP4 study of Arctic Sea ice at 127 ka: sea ice data compilation and model differences. Clim. Past 17 (1), 37–62. https://doi.org/10.5194/cp-17-37-2021.

Karami, M.P., et al., 2021. The role of Arctic gateways on sea ice and circulation in the Arctic and North Atlantic Oceans: a sensitivity study with an ocean-sea-ice model. Clim. Dyn. 57 (7), 2129–2151. https://doi.org/10.1007/s00382-021-05798-6.

Kipp, L.E., et al., 2018. Increased fluxes of shelf-derived materials to the Central Arctic Ocean. Sci. Adv. 4 (1), eaao1302. https://doi.org/10.1126/sciadv.aao1302.

Kipp, L.E., McManus, J.F., Kienast, M., 2021. Radioisotope constraints of Arctic deep water export to the North Atlantic. Nat. Commun. 12 (1), 3658. https://doi.org/10.1038/s41467-021-23877-4.

Kopp, R.E., et al., 2009. Probabilistic assessment of sea level during the last interglacial stage. Nature 462 (7275), 863–867. https://doi.org/10.1038/nature08686.

Krickov, I.V., et al., 2019. Colloidal transport of carbon and metals by western Siberian rivers during different seasons across a permafrost gradient. Geochim. Cosmochim. Acta 265, 221–241. https://doi.org/10.1016/j.gca.2019.08.041.

Krinner, G., et al., 2004. Enhanced ice sheet growth in Eurasia owing to adjacent ice-dammed lakes. Nature 427 (6973), 429–432. https://doi.org/10.1038/nature02233.

Ku, T.L., Broecker, W.S., 1965. Rates of sedimentation in the Arctic Ocean. Prog. Oceanogr. 4, 95–104. https://doi.org/10.1016/0079-6611(65)90043-1.

Ku, T.L., Mathieu, G.G., Knauss, K.G., 1977. Uranium in open ocean: concentration and isotopic composition. Deep-Sea Res. 24 (11), 1005–1017. https://doi.org/10.1016/0146-6291(77)90571-9.

Kuzyk, Z.Z.A., Gobeil, C., Macdonald, R.W., 2013. ^{210}Pb and ^{137}Cs in margin sediments of the Arctic Ocean: controls on boundary scavenging. Glob. Biogeochem. Cycles 27 (2), 422–439. https://doi.org/10.1002/gbc.20041.

Liguori, T.P.B., et al., 2021. The transpolar drift influence on the Arctic Ocean silicon cycle. J. Geophys. Res. Oceans 126 (11). https://doi.org/10.1029/2021JC017352 e2021JC017352.

Lisiecki, L.E., Raymo, M.E., 2005. A Pliocene-Pleistocene stack of 57 globally distributed benthic δ^{18}O records. Paleoceanography 20 (1), PA1003. https://doi.org/10.1029/2004PA001071.

Lisiecki, L.E., Stern, J.V., 2016. Regional and global benthic δ^{18}O stacks for the last glacial cycle. Paleoceanography 31 (10), 1368–1394. https://doi.org/10.1002/2016PA003002.

Lobbes, J.M., Fitznar, H.P., Kattner, G., 2000. Biogeochemical characteristics of dissolved and particulate organic matter in Russian rivers entering the Arctic Ocean. Geochim. Cosmochim. Acta 64 (17), 2973–2983. https://doi.org/10.1016/S0016-7037(00)00409-9.

Luo, Y., Lippold, J., 2015. Controls on ^{231}Pa and ^{230}Th in the Arctic Ocean. Geophys. Res. Lett. 42 (14), 5942–5949. https://doi.org/10.1002/2015GL064671.

Moran, S.B., et al., 2005. ^{231}Pa and ^{230}Th in surface sediments of the Arctic Ocean: implications for ^{231}Pa/^{230}Th fractionation, boundary scavenging, and advective export. Earth Planet. Sci. Lett. 234 (1–2), 235–248. https://doi.org/10.1016/j.epsl.2005.02.016.

Mosher, D.C., Boggild, K., 2021. Impact of bottom currents on deep water sedimentary processes of Canada Basin, Arctic Ocean. Earth Planet. Sci. Lett. 569, 117067 https://doi.org/10.1016/j.epsl.2021.117067.

Niessen, F., et al., 2013. Repeated Pleistocene glaciation of the East Siberian continental margin. Nat. Geosci. 6 (10), 842–846.

Not, C., Hillaire-Marcel, C., 2010. Time constraints from ^{230}Th and ^{231}Pa data in late Quaternary, low sedimentation rate sequences from the Arctic Ocean: an example from the northern Mendeleev Ridge. Quat. Sci. Rev. 29 (25–26), 3665–3675. https://doi.org/10.1016/j.quascirev.2010.06.042.

Not, C., Hillaire-Marcel, C., 2012. Enhanced sea-ice export from the Arctic during the Younger Dryas. Nat. Commun. 3 (1), 647. https://doi.org/10.1038/ncomms1658.

Not, C., et al., 2012. Conservative behavior of uranium vs. salinity in Arctic Sea ice and brine. Mar. Chem. 130, 33–39. https://doi.org/10.1016/j.marchem.2011.12.005.

Nozaki, Y., Horibe, Y., Tsubota, H., 1981. The water column distributions of thorium isotopes in the western North Pacific. Earth Planet. Sci. Lett. 54 (2), 203–216. https://doi.org/10.1016/0012-821X(81)90004-2.

Oppo, D.W., McManus, J.F., Cullen, J.L., 2006. Evolution and demise of the last Interglacial warmth in the subpolar North Atlantic. Quat. Sci. Rev. 25 (23–24), 3268–3277. https://doi.org/10.1016/j.quascirev.2006.07.006.

Osterkamp, T.S., Gosink, J.P., 2013. In: Barnes, P.W., Schell, D.M., Reimnitz, E. (Eds.), The Alaskan Beaufort Sea: Ecosystems and Environments, 82. Academic Press, London. https://doi.org/10.1016/C2013-0-10332-7.

Pavia, F.J., et al., 2020. Isopycnal transport and scavenging of ^{230}Th and ^{231}Pa in the Pacific Southern Ocean. Glob. Biogeochem. Cycles 34 (12). https://doi.org/10.1029/2020GB006760 e2020GB006760.

Pearce, C., et al., 2017. The 3.6 ka Aniakchak tephra in the Arctic Ocean: a constraint on the Holocene radiocarbon reservoir age in the Chukchi Sea. Clim. Past 13 (4), 303–316. https://doi.org/10.5194/cp-13-303-2017.

Pico, T., et al., 2020. Recent constraints on MIS 3 sea level support role of continental shelf exposure as a control on Indo-Pacific hydroclimate. Paleoceanogr. Paleoclimatol. 35 (8) https://doi.org/10.1029/2020PA003998 e2020PA003998.

Pokrovsky, O.S., et al., 2014. Fate of colloids during estuarine mixing in the Arctic. Ocean Sci. 10 (1), 107–125. https://doi.org/10.5194/os-10-107-2014.

Polyak, L., et al., 2001. Ice shelves in the Pleistocene Arctic Ocean inferred from glaciogenic deep-sea bedforms. Nature 410 (6827), 453–457. https://doi.org/10.1038/35068536.

Poore, R.Z., et al., 1999a. Late Pleistocene and Holocene meltwater events in the western Arctic Ocean. Geology 27 (8), 759–762. https://doi.org/10.1130/0091-7613(1999)027%3C0759:LPAHME%3E2.3.CO;2.

Poore, R.Z., Ostermann, D.R., McGeehin, J., 1999b. Stable isotope data and AMS ^{14}C dates from Arctic Ocean Section 1994 surface sediment transect and box core samples from the Mendeleyev Ridge area. US Department of the Interior, US Geological Survey.

Purcell, K., et al., 2022. Potential and limitation of ^{230}Th-excess as a chronostratigraphic tool for late Quaternary Arctic Ocean sediment studies: an example from the Southern Lomonosov Ridge. Mar. Geol. 448, 106802 https://doi.org/10.1016/j.margeo.2022.106802.

Rasmussen, T.L., et al., 2003. Late warming and early cooling of the sea surface in the Nordic seas during MIS 5e (Eemian Interglacial). Quat. Sci. Rev. 22 (8–9), 809–821. https://doi.org/10.1016/S0277-3791(02)00254-8.

Raymo, M.E., et al., 2018. The accuracy of mid-Pliocene δ^{18}O-based ice volume and sea level reconstructions. Earth-Sci. Rev. 177, 291–302. https://doi.org/10.1016/j.earscirev.2017.11.022.

Reimer, P.J., et al., 2013. IntCal13 and Marine13 radiocarbon age calibration curves 0–50,000 years cal BP. Radiocarbon 55 (4), 1869–1887. https://doi.org/10.2458/azu_js_rc.55.16947.

Richards, A.E., et al., 2022. Spatial and temporal variability of Atlantic Water in the Arctic from 40 years of observations. Geophys. Res. Oceans 127, e2021JC018358. https://doi.org/10.1029/2021JC018358.

Rippeth, T., Fine, E., 2022. Turbulent mixing in a changing Arctic Ocean. Oceanography 35 (2). https://doi.org/10.5670/oceanog.2022.103.

Roca Martí, M., 2017. Carbon export from the upper water column of the polar oceans by using natural radionuclides. PhD Thesis. Universitat Autònoma de Barcelona, Cerdanyola del Vallès.

Rogge, A., et al., 2022. Carbon dioxide sink in the Arctic Ocean from cross-shelf transport of dense Barents Sea water. Nat. Geosci. 16, 82–88 https://doi.org/10.1038/s41561-022-01069-z.

Roy-Barman, M., 2009. Modelling the effect of boundary scavenging on Thorium and Protactinium profiles in the ocean. Biogeosciences 6 (12), 3091–3107. https://doi.org/10.5194/bg-6-3091-2009.

Rudels, B., 2011. Arctic Ocean circulation and variability-advection and external forcing encounter constraints and local processes. Ocean Sci. Discuss. 8 (2), 261–286. https://doi.org/10.5194/os-8-261-2012.

Rudels, B., et al., 2012. Observations in the ocean. In: Lemke, P., Jacobi, HW. (Eds.). In: Arctic Climate Change, 43. Springer, Dordrecht, pp. 117–198. doi:org/10.1007/978-94-007-2027-5_4.

Rudels, B., Carmack, E., 2022. Arctic Ocean water mass structure and circulation. Oceanography 35 (3/4), 52–65.

Scholten, J.C., Van Der Loeff, M.M.R., Michel, A., 1995. Distribution of ^{230}Th and ^{231}Pa in the water column in relation to the ventilation of the deep Arctic basins. Deep-Sea Res. II Top. Stud. Oceanogr. 42 (6), 1519–1531. https://doi.org/10.1016/0967-0645(95)00052-6.

Schulz, K., et al., 2021. Turbulent mixing and the formation of an intermediate nepheloid layer above the Siberian continental shelf break. Geophys. Res. Lett. 48 (9) https://doi.org/10.1029/2021GL092988 e2021GL092988.

Somayajulu, B.L.K., Sharma, P., Herman, Y., 1989. Thorium and uranium isotopes in Arctic sediments. In: Herman, Y. (Ed.), The Arctic Seas. Springer, Boston, MA, pp. 571–579. https://doi.org/10.1007/978-1-4613-0677-1_22.

Song, T., et al., 2022a. Sedimentology, Mineralogy, and Geochemistry Results of Core Arc7-E25 from Southern Mendeleev Ridge, Arctic Ocean. PANGAEA. https://doi.org/10.1594/PANGAEA.949846.

Song, T., et al., 2022b. A reassessment of Nd-isotopes and clay minerals as tracers of the Holocene Pacific water flux through Bering Strait. Mar. Geol. 443, 106698 https://doi.org/10.1016/j.margeo.2021.106698.

Spielhagen, R.F., et al., 2022. No freshwater-filled glacial Arctic Ocean. Nature 602 (7895), E1–E3. https://doi.org/10.1038/s41586-021-04089-8.

Stein, R., 2008. Arctic Ocean Sediments: Processes, Proxies, and Paleoenvironment. In: Chamley, H. (Ed.), Developments in Marine Geology. Elsevier, Oxford.Elsevier, pp. 82–83.

Stein, R., et al., 2017. Arctic Ocean sea ice cover during the penultimate glacial and the last interglacial. Nat. Commun. 8 (1), 373. https://doi.org/10.1038/s41467-017-00552-1.

Strobl, C., 1998. Datierung von Sedimentkernen und Rekonstruktion der Transportwege der Radionuklide ^{10}Be, ^{230}Th und ^{231}Pa in hohen nördlichen Breiten. PhD Thesis. Ruprecht-Karls-Universität, Heidelberg.

Suman, D.O., Bacon, M.P., 1989. Variations in Holocene sedimentation in the North American Basin determined from ^{230}Th measurements. Deep Sea Res. Part I Oceanogr. Res. Pap. 36 (6), 869–878. https://doi.org/10.1016/0198-0149(89)90033-2.

Trimble, S.M., Baskaran, M., Porcelli., D., 2004. Scavenging of thorium isotopes in the Canada Basin of the Arctic Ocean. Earth Planet. Sci. Lett. 222 (3–4), 915–932. https://doi.org/10.1016/j.epsl.2004.03.027.

Valk, O., et al., 2018. Importance of hydrothermal vents in scavenging removal of ^{230}Th in the Nansen Basin. Geophys. Res. Lett. 45 (19), 10539–10548. https://doi.org/10.1029/2018GL079829.

Valk, O., et al., 2020. Decrease in ^{230}Th in the Amundsen Basin since 2007: far-field effect of increased scavenging on the shelf? Ocean Sci. 16 (1), 221–234. https://doi.org/10.5194/os-16-221-2020.

Van Nieuwenhove, N., Bauch, H.A., 2008. Last interglacial (MIS 5e) surface water conditions at the Vøring Plateau (Norwegian Sea), based on dinoflagellate cysts. Polar Res. 27 (2), 175–186. https://doi.org/10.1111/j.1751-8369.2008.00062.x.

Vetrov, A.A., Romankevich, E.A., 2019a. Distribution, fluxes, and balance of particulate organic carbon in the Arctic Ocean. Oceanology 59 (4), 491–499. https://doi.org/10.1134/S0001437019040180.

Vetrov, A.A., Romankevich, E.A., 2019b. Distribution and fluxes of dissolved organic carbon in the Arctic Ocean. Polar Res. 38, 3500. https://doi.org/10.33265/polar.v38.3500.

Wefing, A.M., et al., 2020. Circulation timescales of Atlantic Water in the Arctic Ocean determined from anthropogenic radionuclides. Ocean Sci. 17 (1), 111–129. https://doi.org/10.5194/os-17-111-2021.

Wegner, C., et al., 2015. Variability in transport of terrigenous material on the shelves and the deep Arctic Ocean during the Holocene. Polar Res. 34 (1), 24964. https://doi.org/10.3402/polar.v34.24964.

Weigelt, E., Jokat, W., Eisermann, H., 2020. Deposition history and paleo-current activity on the Southeastern Lomonosov Ridge and its Eurasian Flank based on seismic data. Geochem. Geophys. Geosyst. 21 (11) https://doi.org/10.1029/2020GC009133 e2020GC009133.

West, G., et al., 2023. Amino acid racemization in Neogloboquadrina pachyderma and Cibicidoides wuellerstorfi from the Arctic Ocean and its implications for age models. Geochronology 5 (1), 285–299. https://doi.org/10.5194/gchron-5-285-2023.

Wetterich, S., et al., 2016. Ice complex permafrost of MIS5 age in the Dmitry Laptev Strait coastal region (East Siberian Arctic). Quat. Sci. Rev. 147, 298–311. https://doi.org/10.1016/j.quascirev.2015.11.016.

Wetterich, S., et al., 2020. The cryostratigraphy of the Yedoma cliff of Sobo-Sise Island (Lena delta) reveals permafrost dynamics in the Central Laptev Sea coastal region during the last 52 kyr. Cryosphere 14 (12), 4525–4551. https://doi.org/10.5194/tc-14-4525-2020.

Wheeler, P.A., et al., 1996. Active cycling of organic carbon in the Central Arctic Ocean. Nature 380 (6576), 697–699. https://doi.org/10.1038/380697a0.

Williford, T., et al., 2022. Spatial complexity in dissolved organic matter and trace elements driven by hydrography and freshwater input across the Arctic Ocean during 2015 Arctic GEOTRACES expeditions. J. Geophys. Res. Oceans 127. https://doi.org/10.1029/2022JC018917 e2022JC018917.

Woodgate, R.A., et al., 2001. The Arctic Ocean boundary current along the Eurasian slope and the adjacent Lomonosov Ridge: water mass properties, transports and transformations from moored instruments. Deep Sea Res. Part I Oceanogr. Res. Pap. 48 (8), 1757–1792. https://doi.org/10.1016/S0967-0637(00)00091-1.

Xiang, Y., Lam, P.J., 2020. Size-fractionated compositions of marine suspended particles in the Western Arctic ocean: lateral and vertical sources. J. Geophys. Res. Oceans 125 (8). https://doi.org/10.1029/2020JC016144 e2020JC016144.

Xiao, X., Stein, R., Fahl, K., 2015. MIS 3 to MIS 1 temporal and LGM spatial variability in Arctic Ocean sea ice cover: reconstruction from biomarkers. Paleoceanography 30 (7), 969–983. https://doi.org/10.1002/2015PA002814.

Xiao, W., et al., 2021. A sedimentary record from the Makarov Basin, Arctic Ocean, reveals changing middle to Late Pleistocene glaciation patterns. Quat. Sci. Rev. 270, 107176 https://doi.org/10.1016/j.quascirev.2021.107176.

Xiao, W., et al., 2022. Reply to comment by Hillaire-Marcel and de Vernal on "A sedimentary record from the Makarov Basin, Arctic Ocean, reveals changing middle to late Pleistocene glaciation patterns"[Quat. Sci. Rev., 270 (2021), p. 107176]. Quat. Sci. Rev. 276, 107298. https://doi.org/10.1016/j.quascirev.2021.107298.

Xu, Q., et al., 2021. Driving mechanisms of sedimentary ^{230}Th and ^{231}Pa Variability in the Western Arctic Ocean through the last Glacial Cycle. Paleoceanogr. Paleoclimatol. 36 (7) https://doi.org/10.1029/2020PA004039 e2020PA004039.

Yang, H.S., et al., 1986. The distribution of ^{230}Th and ^{231}Pa in the deep-sea surface sediments of the Pacific Ocean. Geochim. Cosmochim. Acta 50 (1), 81–89. https://doi.org/10.1016/0016-7037(86)90050-5.

Ye, L., et al., 2020. Ice events along the East Siberian continental margin during the last two glaciations: evidence from clay minerals. Mar. Geol. 428, 106289 https://doi.org/10.1016/j.margeo.2020.106289.

Zhang, X., et al., 2021. Adsorption of Th and Pa onto particles and the effect of organic compounds in natural seawater. J. Oceanol. Limnol. 39 (6), 2209–2219. https://doi.org/10.1007/s00343-021-0297-5.

Zimmermann, H.H., et al., 2017. Sedimentary ancient DNA and pollen reveal the composition of plant organic matter in Late Quaternary permafrost sediments of the Buor Khaya Peninsula (north-eastern Siberia). Biogeosciences 14 (3), 575–596. https://doi.org/10.5194/bg-14-575-2017.